Graduate thesis

NTNU
Norwegian University of Science and Technology
Faculty of Natural Sciences
Department of Biotechnology and Food Science

Pelle Jensen

A Comparative Analysis of Rheometer and Pipe Rig Methods for Rheological Characterization of Microfibrillated Cellulose Suspensions as a Model Fluid for Wastewater Sludge

Graduate thesis in Chemical Engineering and Biotechnology
Supervisor: Kurt I. Draget, Størker Moe
Co-supervisor: Alexandru Botan (Cambi), Erik Tylleskär (Cambi)
June 2023

NTNU
Norwegian University of Science and Technology

Pelle Jensen

A Comparative Analysis of Rheometer and Pipe Rig Methods for Rheological Characterization of Microfibrillated Cellulose Suspensions as a Model Fluid for Wastewater Sludge

Graduate thesis in Chemical Engineering and Biotechnology
Supervisor: Kurt I. Draget, Størker Moe
Co-supervisor: Alexandru Botan (Cambi), Erik Tylleskär (Cambi)
June 2023

Norwegian University of Science and Technology
Faculty of Natural Sciences
Department of Biotechnology and Food Science

NTNU
Norwegian University of
Science and Technology

Acknowledgement

I would like to express my sincere appreciation to the individuals who have played a crucial role in the completion of my master's thesis in Chemical Engineering and Biotechnology at the Norwegian University of Science and Technology (NTNU) in Trondheim.

I am deeply grateful to my supervisors, Kurt Ingar Draget and Størker Moe from NTNU, for their invaluable guidance and support. Their expertise in rheology and fluid dynamics has greatly enhanced my understanding of the subject matter, and their detailed feedback has significantly improved the quality of this thesis.

I would also like to extend my thanks to Erik Tylleskär and Alexandru Botan from Cambi for their valuable contributions. Erik's practical guidance in organizing the experimental work, particularly with the pipe rig, was central to the successful execution of the project. Alexandru's theoretical assistance, spanning various areas such as optimization, statistics, and theory, greatly enriched the depth and thoroughness of this research.

I would like to express my heartfelt appreciation to my girlfriend, Camilla, for her unwavering support and patience throughout this research journey. Her understanding and encouragement during times of frustration and delays have been immensely valuable in keeping me motivated.

Lastly, I want to acknowledge the support of my friends Stian Ringbakken Stenhaug and Tobias Borthen, making up two-thirds of our "Bio-Trio". Sitting next to each other in the study hall provided much-needed moments of fun and motivation. Shared breaks allowed for support and inspiration during challenging times.

I extend my gratitude to all those mentioned above, as well as anyone else who may have contributed in their own way. Without their support, this thesis would not have been possible.

Abstract

In the pursuit of optimizing material handling processes, gaining a thorough understanding of material behavior and its underlying properties is crucial. Among these properties, the apparent viscosity holds a pivotal role in estimating the energy required for efficient transportation within a processing plant. This thesis aims to assess the viability of using a laboratory rheometer to analyze the flow behavior of sewage sludge in pipes. The utilization of Exilva, a microfibrillated cellulose, as a model fluid for wastewater sludge, is suggested to facilitate a more convenient and consistent exploration of flow properties.

This project further focuses on establishing a reliable and reproducible technique for obtaining rheological data using a laboratory rheometer. Initially, experiments were conducted on Newtonian fluids to develop and verify the method, which was subsequently adjusted to accommodate non-Newtonian fluids. The method involves determining the effective dimensions of vane geometries and employing non-Newtonian correction factors to calculate shear rate and shear stress across the vane-to-container gap. The resulting flow data were fitted numerically to the Herschel-Bulkley non-Newtonian rheology model. Consistent rheometer results were obtained for concentrations up to 2.44%, while higher concentrations exhibited highly complex behavior.

To capture realistic flow behavior, a pipe testing rig was constructed to gather data on Exilva suspensions in pipes. These data were then fitted numerically to the Herschel-Bulkley model to estimate flow parameters. To assess the feasibility of using a laboratory-scale rheometer for estimating fluid flow in pipes, a comparison was made between the rheometer and pipe rig methods. For lower-concentration materials, both rheometer apparent viscosity and pipe rig measurements yielded similar outcomes when applying the Herschel-Bulkley model. However, notable discrepancies arose when dealing with higher-concentration materials, indicating challenges in accurately characterizing their rheological properties.

Sammendrag

I jakten på å optimalisere materialhåndteringsprosesser er det avgjørende å få en grundig forståelse av materialers underliggende egenskaper. Blant disse egenskapene spiller viskositeten en sentral rolle i å estimere energien som kreves for effektiv transport i et prosessanlegg. Denne oppgaven tar sikte på å vurdere muligheten til å bruke et laboratoriereometer for å analysere strømningsatferden til kloakkslam i rør. Bruken av Exilva, en mikrofibrillert cellulose, som et modellfluid for avløpsslam, foreslås for å muliggjøre en mer praktisk og konsistent utforskning av strømningsegenskapene.

Dette prosjektet fokuserer på å etablere en pålitelig og reproduserbar metode for innhenting av reologiske data ved bruk av et laboratoriereometer. Først ble det utført eksperimenter på newtonske væsker for å utvikle og verifisere metoden, som deretter ble justert for å imøtekomme ikke-newtonske væsker. Metoden innebærer å bestemme de effektive dimensjonene til vane-geometrier og bruke ikke-newtonske korreksjonsfaktorer for å beregne skjærhastighet og skjærspenning over mellomrummet mellom vane-geometrien og beholderen. De resulterende strømningsdata ble numerisk tilpasset til en Herschel-Bulkley ikke-newtonsk reologimodell. Konsistente resultater fra reometeret ble oppnådd for konsentrasjoner opp til 2,44%, mens høyere konsentrasjoner viste svært kompleks oppførsel.

For å undersøke realistisk strømningsatferd, ble det konstruert en rør-rigg for å samle data om strømning av Exilva i rør. Disse dataene ble deretter numerisk tilpasset til Herschel-Bulkley-modellen for å estimere strømningsparametere. For å vurdere muligheten til å bruke et laboratorieskala-reometer til å estimere væskestrøm i rør, ble det foretatt en sammenligning mellom reometer- og rørriggmetoden. For materialer med lavere konsentrasjon ga både reometermålinger og rørriggmålinger lignende resultater ved bruk av Herschel-Bulkley-modellen. Imidlertid oppsto det bemerkelsesverdige avvik når det gjelder materialer med høyere konsentrasjon, noe som indikerer utfordringer med å nøyaktig karakterisere deres reologiske egenskaper.

Contents

1 List of abbreviations

Table 1.1: List of abbreviations for general parameters.

Symbol	Explanation
Ramp test	Controlled shear rate test
MFC	Microfibrillated cellulose
ρ	Density $[kgm^{-3}]$
N_{Re}	Reynolds number $[-]$
N_{Re_3}	Revised Reynolds number $[-]$
K	Flow consistency index $[Pa\ s^n]$
n	Flow behavior index $[-]$
DS	Dry solids content $[\% = \frac{gDS}{gsample}]$

Table 1.2: List of abbreviations for flow in pipes.

Symbol	Explanation
σ	Shear stress $[Nm^{-2} = Pa]$
τ_0	Shear stress at wall (pipe) $[Nm^{-2} = Pa]$
τ_y	yield stress $[Nm^{-2} = Pa]$
η	Shear viscosity $[Pa\ s]$
$\eta_{apparent}$	Apparent viscosity $[Pa\ s]$
ν	Average fluid flow velocity $[ms^{-1}]$
μ	Fluid viscosity $[Pa\ s]$
N_{Re}	Reynolds number $[-]$
N_{Re_3}	Revised Reynolds number $[-]$
V_{ann}	Average fluid flow velocity in annulus $[ms^{-1}]$
D_{shear}	Thickness of sheared zone (annulus) $[m]$
D_{plug}	Diameter of plug $[m]$
r_{plug}	radius of plug $[m]$
R	Radius of pipe $[m]$
D	Diameter of pipe $[m]$
Q	Volumetric flow rate in pipe $[m^3s^{-1}]$
Q_{plug}	volumetric flow rate in the plug $[m^3s^{-1}]$
A_{plug}	cross-sectional area of the plug$[m^2]$
u_{plug}	plug velocity $[m/s]$
Q_{ann}	volumetric flow rate in the annulus $[m^3s^{-1}]$
A_{ann}	cross-sectional area of the annulus $[m^2]$
Δp_f	Pressure loss due to friction $[Pa]$
L	Length of pipe $[m]$
F_f	Mechanical energy loss due to friction [Nm/kg]
τ_s	Shear stress at pipe wall $[Nm^{-2} = Pa]$
f	Fanning friction factor

Table 1.3: List of abbreviations for rheometer testing.

Symbol	Explanation
τ	Shear stress $[Nm^{-2} = Pa]$
σ	Shear stress $[Nm^{-2} = Pa]$
σ_1	Shear stress at inner cylinder $[Nm^{-2} = Pa]$
τ_0	yield stress $[Nm^{-2} = Pa]$
η	Shear viscosity $[Pa\ s]$
$\eta_{apparent}$	Apparent viscosity $[Pa\ s]$
$\eta_{corrected}$	Corrected viscosity $[Pa\ s]$
$\dot{\gamma}$	Shear rate $[s^{-1}]$
R_1	Inner cylinder radius $[m]$
R_2	Outer cylinder radius $[m]$
F_σ	Shear stress factor $[m^{-3}]$
$F_{\dot{\gamma}}$	Shear rate factor $[-]$
H	Effective height $[m]$
y	Non-wetted height $[m]$
h	Immersed height $[m]$
Ω	Angular velocity $[s^{-1}]$
Γ	Torque $[Nm]$
C	Rheometer friction $[Nms]$
s	Ratio between R_2 and R_1 $[-]$
C_R	Correction factor $[-]$

2 Introduction

2.1 Aim

The primary objective of this master's thesis is to determine the feasibility of utilizing a laboratory rheometer to characterize the flow of sewage sludge in pipes. In addition, suspensions of microfibrillated cellulose (MFC) were employed as model fluids for experimental analysis.

Extensive data analysis and literature review showed that inconsistencies were found in the viscosity data of the preliminary work. Substantial effort was put into establishing a reliable method to obtain satisfactory and consistent rheological data for Newtonian and non-Newtonian fluids. Correction factors were computed to establish well-grounded experimental methods. These methods were used in this thesis as well as it is useful for further research.

The research is focused on establishing a dependable and reproducible technique for obtaining rheological data with a laboratory rheometer. Moreover, the critical element is to develop a model fluid with similar rheological characteristics to wastewater sludge to facilitate testing and comparison with a pipe testing rig. At the end of this project, the value and usefulness of using laboratory rheometers to characterize the flow of non-Newtonian shear-thinning fluids in pipes will be established.

Originally, the primary objective of this study was to comprehensively characterize and enhance the understanding of the flow behavior of sewage sludge. However, due to the inherent instability of sewage sludge and the influence of biogas production on its rheological properties, conducting direct testing using sludge proved challenging. To overcome this obstacle, a model fluid was employed and thoroughly evaluated to establish reliable experimental methodologies.

Subsequently, it was recognized that the initial scope of the research was overly broad. Thus, the focus of the thesis was refined to concentrate solely on conducting experiments involving MFC suspensions. This adjustment was motivated by previous findings that indicated remarkable similarities in flow behavior between sewage sludge and suspensions of MFC. Consequently, MFC served as a suitable surrogate for sludge, facilitating a more targeted investigation into flow characteristics and associated phenomena.

2.2 Importance of rheology for process equipment design

At large industrial plants, materials may undergo multiple treatment steps, leading to significant alterations in their rheological properties and subsequent changes in flow behavior throughout processing. A comprehensive understanding of the material behavior and underlying properties are essential in the process of optimizing material handling processes. In particular, the apparent viscosity plays a critical role in estimating the required energy for transport in processing

plants. Moreover, rheology is a crucial and major factor when designing and sizing equipment such as pipelines, pumps, and heat exchangers.

3 Previous work and importance for this thesis

As a preparation for this master's thesis, a 15 ECTS points project was conducted as a precursor. The project included in-detail theory about wastewater sludge, Newtonian and non-Newtonian fluids, non-Newtonian rheology models, and methods in which non-Newtonian fluids are characterized. The intent of this section is to summarize the most important theory from the study project. In addition, it offers a background for understanding this thesis itself, and the structuring of the methodology. This summary also contains a brief presentation of the initial results and conclusions from the previous work, to support the theory and the choice of microfibrillated cellulose suspensions as a model fluid for wastewater sludge.

Wastewater sludge is a non-Newtonian fluid, meaning that the ratio between shear stress and shear rate is not constant. As a result of this, the viscosity changes with the shear rate. Wastewater sludge is shear thinning, meaning that the viscosity decreases with increasing shear rates. The Herschel-Bulkley model was found to give sufficient accuracy, while still being simple enough to compute effectively.

From an extensive literature review, it was found that the apparent viscosity of wastewater sludge increases with the increasing content of dry solids. The same case is evident for yield stress. Increasing temperature decreases both apparent viscosity and yield stress while increasing pH values leads to increased viscosity and yield stress. Further, the effect of chemical oxygen demand and particle size distribution was reviewed. Increasing chemical oxygen demand seemed to lead to increasing apparent viscosity. A negative correlation between sludge viscosity and the concentration of extracellular polymeric substances showed that large flocs lead to lower apparent viscosity.

Earlier studies conducted on microfibrillated cellulose suspensions showed that the material had similar rheological behavior as wastewater sludge. Rheometer testing with a vane geometry was used to compare the two materials. Both materials showed comparable shear thinning behavior, which was modelable by the Herschel-Bulkley model. In addition, the microfibrillated cellulose showed a positive relationship between concentration and viscosity, thus making it possible to iterate through concentrations to find one that resulted in flow curves that were easily compared to sludge.

A rotational rheometer equipped with different size vane geometries was used to carry out the experimental work. The vane geometry has proven to be effective when testing fluids where slippage may occur at the container well. This makes it suitable for testing on thick fluids with high levels of particles, such as wastewater sludge. The rheometer was rotated at given speeds while measuring the torque needed to maintain the specified speed.

All findings relevant to this master's thesis are summarized in the following list.

- Wastewater sludge
  - Non-Newtonian shear thinning
  - Time-dependent shear thinning behavior (thixotropic)
  - Can be modeled by the Herschel-Bulkley model
  - Viscosity and yield stress increase with increased dry solids content
  - Viscosity and yield stress decrease with increased temperature
  - Viscosity and yield stress increase with increased pH
  - Viscosity increase with increased COD
  - Viscosity decrease with increased floc size
- Microfibrilated cellulose
  - Non-Newtonian shear thinning
  - Can be modeled by the Herschel-Bulkley model
  - Viscosity increase with increased dry solids content
  - Similar rheological behavior to wastewater sludge

Complications with the results were encountered, as the equipment yielded dissimilar viscosities when equipped with different vane geometries. Consequently, a large part of this Master's thesis aims to investigate and correct data while establishing a reliable method for benchtop scale rheometer testing with vane geometries.

The previous work *Rheological characterization of sludge from wastewater treatment plants compared to microfibrillated cellulose suspensions*, Pelle Jensen, December 2022[1], is attached to the delivery of this master's thesis.

The previous work summarized in this section played an important role as a preliminary study of this thesis. The initial test results were used as a guideline for finding correction factors of uttermost importance, as well as establishing a reliable model fluid for further testing, both in lab-scale and pilot-scale facilities.

4 Theory

4.1 Fluids

In general, there are two types of fluids, Newtonian and non-Newtonian. Newtonian fluids obey Newton's law of constant viscosity, meaning that the viscosity is independent of shear rate and that the material holds no yield stress. Conversely, this is not the case for non-Newtonian fluids. When non-Newtonian fluids are exposed to mechanical stress, the ratio between shear rate and shear stress is non-constant, which results in non-constant viscosity [2], and thus the term apparent viscosity is introduced [3]. Some non-Newtonian fluids exhibit yield stress. Some diluted sludges may show Newtonian behavior, but thicker sludges that have been dewatered at wastewater treatment plants, show non-Newtonian behavior where the viscosity is dependent on the shear rate [4].

4.2 Wastewater sludge

Wastewater is generated from both domestic uses of water, commercial establishments, and industries. Because of this, the wastewater characteristics may have large variations from place to place [5]. Wastewater sludge refers to the solid material that is generated and separated from water during the treatment of sewage liquids at wastewater treatment plants. The sludge is a mixture of various organics and inorganics, including microorganisms. [6]. Sludge is a complex material, and the rheological properties of wastewater sludge have proven hard to describe precisely [7].

The preliminary study of this thesis found, in accordance with theory, that wastewater sludge is non-Newtonian and shear thinning [3] [8] [7]. Further, sludge shows time-dependent shear thinning, thixotropic, behavior [9] [10] [11].

4.3 Model fluid

To investigate the suitability of a laboratory rheometer for predicting the flow behavior of sludge in pipes, a model fluid was employed. The methodology of both the rotational rheometer and pip rig was verified by measuring the properties of a model fluid with known and more constant rheological characteristics.

A microfibrillated cellulose (MFC) product was the chosen model fluid for this thesis. The product is called Exilva and is manufactured and sold by Borregaard. Exilva is a highly viscous fluid [12], and it exhibits non-Newtonian behavior with a shear-thinning effect at higher shear rates [13]. Further, Exilva exhibits a yield stress, requiring a given minimum force for it to start moving. Some MFC suspensions also display time-dependent thixotropic behavior [14]. All these characteristics are consistent with the behavior of sludge from wastewater treatment plants. As for sludge, the concentration of MFC dispersions influences the yield stress and viscosity of the fluids, with higher concentrations resulting in increased yield stress and viscosity [14].

Dynamic oscillatory measurements conducted on sludge have shown that the viscoelastic behavior of digested sludge shares similarities with that of soft glassy materials[15]. This includes pastes, emulsions, and slurries, which exhibit complex flow properties under mechanical stress[16]. Similar viscoelastic behavior suggests that soft glassy materials like Exilva can act as a model fluid for wastewater sludge.

4.4 Characterizing fluids with rheometers

Rheometers are scientific instruments employed in laboratories for evaluating flow curves of Newtonian and non-Newtonian fluids. Flow curves describe the correlation between stress and strain in fluids[3]. The rheometer inspects the response of fluid when exposed to an applied force, which is introduced by the rotation of the rheometer. Rheometers are often used for analyzing non-Newtonian fluids where basic viscometers are inadequate due to variable apparent viscosity.

Certain advanced rotational rheometers have the ability to operate under a controlled shear rate, which entails a predefined rotational speed, or controlled shear stress, which involves a predetermined torque. For these measurements, the preestablished parameter is the independent variable, supplying the opposite parameter as dependent. The rotational speed, angular velocity, and torque are then recalculated to shear rate and shear stress, respectively[17]. These parameters are then translated to apparent viscosity as the ratio between shear stress and shear rate[2]. In order to meet particular fluid-dependent criteria, rotational rheometers can be equipped with different spindle geometries. This thesis mainly utilizes a rotational rheometer from Brookfield, which is further described in detail in section 5.1.

4.4.1 Rheometer geometries

Multiple geometries exist for use with given fluids. Popular geometries include vane, bob-in-cup, cone-plate, plate-plate, and double concentric. The vane geometry as well as necessary calculations are explained in detail in section 4.5.

Common for all of the geometries, either a predefined torque or rotation speed is used to measure and calculate the resulting shear rate and shear stress. Further computation of the data leads to the apparent viscosity as the ratio of shear stress to shear rate[18][19].

The bob-in-cup geometry involves a cylindrical bob rotating inside a coaxial cylindrical cup[19], with the material placed in the annulus between the bob and the cup. The bob-in-cup geometry is usually found in two variations, the pointed bob, and a concentric cylinder. The gap between the bob and the cup is small, thus making it possible to calculate the shear rate distribution and further calculation the apparent viscosity[18]. The concentric cylinder geometry is shown in figure 4.1.

The cone-plate and plate-plate geometries consist of either a rotating cone or plate at the top and a stationary plate at the bottom. The sample is placed on the lower plate before the top geometry is lowered down on the material. The gap between the two geometries is low, usually less than 1000 μm, but dependent on the thickness of the material[18]. The small gap initiates capillary forces which keep the material in place while the top geometry is rotating[20]. The cone-plate and plate-plate geometries are shown in figure 4.1.

Double concentric geometry is mainly used when the structure of the surface varies from the structure of the bulk fluid[18]. The geometry significantly reduces the wall-slip effect, making it a favorable option when conducting rheological experiments on complex samples, such as sludge[21]. An example of the double concentric geometry is shown in figure 4.1.

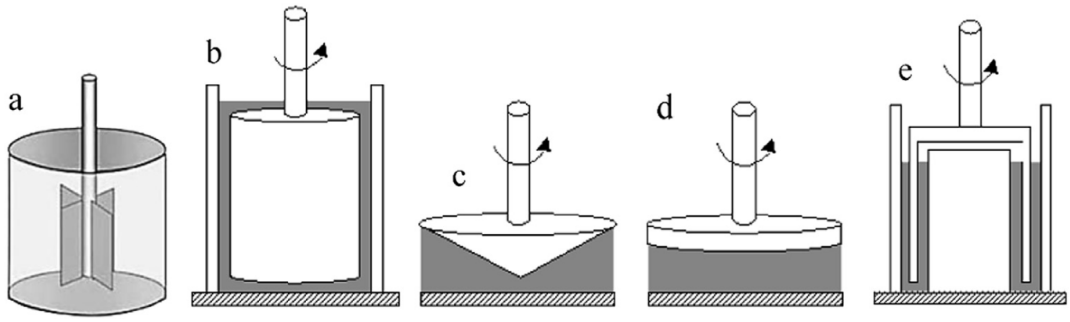

Figure 4.1: Popular geometries used with rotational rheometers with examples of a) vane, b) concentric cylinder, c) cone-plate, d) plate-plate, e) double concentric[3].

4.5 Vane geometry and analysis

4.5.1 Vane geometry

The vane geometry for rheometers consists of an impeller attached to a shaft. The impeller may be composed of multiple blades where two, three, four, or six blades are the most popular[22]. The blade is submerged into a sample in a container, and the shaft is slowly rotated by a motor in the rheometer to measure the needed torque for a predefined rotating speed[23][19]. Vane geometries are often preferred with fluids that show slippage at the edge[24]. This effect is often seen with thick fluids with a high concentration of particles[23]. The sample volume needed to use the vane geometry is determined by the size of the vane and the test container. An example of the vane geometry is shown in figure 4.1.

4.5.2 Vane geometry as an effective cylinder

Calculating shear rate and shear stress distributions across the gap between the vane edge and container is the main challenge when using vane geometries[25]. In order to do this, geometric factors which translate the torque and angular velocity from the rheometer to shear stress and shear rate, respectively, have to be

determined. A common way of determining the shear stress factor is to assume the vane to be a cylinder with an effective cylinder height and radius[26]. This hypothesis is predicated on the supposition that the material becomes entrapped within the region between the vane blades[27][28]. The dimensions of the theoretical effective cylinder are assumed to be close to that of the vane, however, it has to be determined for each specific vane[26].

Visualization of streamlines forming from a vane rotating in a liquid would give indications of the expected effective dimensions. Figure 4.2 shows streamlines around a vane that is rotating at an angular velocity of $0.5 rad/s$ in glycerin with a viscosity of $1.37 Pas$[25]. The fluid patterns exhibit polygonal shapes in close proximity to the blade edges, followed by a swift transition towards a circular form as they move further away from the vane edge. The progression from a polygonal shape to a circular shape is dependent on the location of the outer container, i.e. the gap size between the vane edge and container, but it shows that a cylindrical geometry may be used as a feasible approximation for a vane[25]. The presence of polygonal-shaped streamlines suggests that the suitable effective radius for an analogous cylinder should fall within the range of a circle inscribed within the polygon's sides and the radius of a circle inscribed within the vane's actual radius[29].

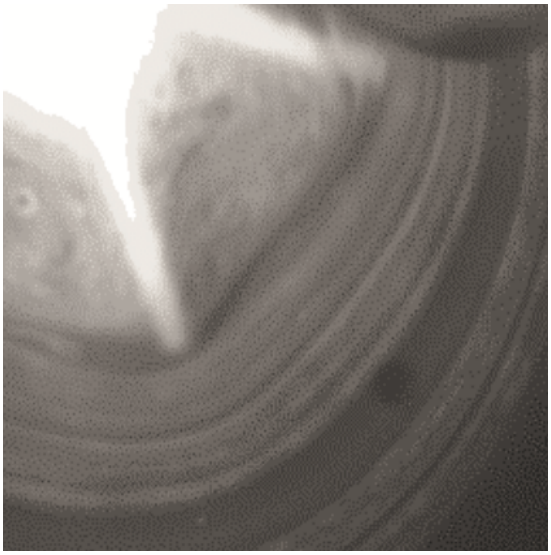

Figure 4.2: Streamlines around a vane rotating at an angular velocity of $0.5 rad/s$ in glycerin with a viscosity of $1.37 Pa\ s$. The picture is from Baravian, Lalante & Parker[25].

4.5.3 Determination of dimensions of an effective equivalent cylinder

A method of determining the effective dimensions of a vane is the method of partial immersion[25]. The method involves submersion of a vane to different depths, and then measuring the required torque at different predefined angular velocities. This way, the required torque can be measured as a function of the submersion depth of the vane[30]. Measurements are conducted on Newtonian

fluids to have a consistent viscosity independent of angular velocity.

For a concentric cylinder, the shear stress factor, $F_\sigma[m^{-3}]$, is the ratio of shear stress at the inner cylinder, $\sigma_1[Pa]$, and torque, $\Gamma[Nm]$. When the diffusion of vorticity is constant, the shear stress factor is constant for all materials. Constant diffusion of vorticity entails that the shear stress distribution is known, as seen in equation (4.1) [25].

$$\sigma = \frac{\sigma_1 R_1^2}{r^2} \tag{4.1}$$

Where σ is the shear stress $[Pa]$ at a given distance from the inner cylinder, $r[m]$, and R_1 is the inner cylinder radius $[m]$. The shear stress factor is independent with respect to the sample and relies solely on the geometry. The shear stress factor is calculated as shown in equation (4.2) [25].

$$F_\sigma = \frac{1}{2\pi R_1^2 h} \tag{4.2}$$

Where h is the immersed length of the geometry $[m]$.

The shear rate factor, $F_{\dot{\gamma}}$ $[-]$, is the ratio between the shear rate, $\dot{\gamma}$ $[1/s]$, and angular velocity, Ω $[1/s]$, at the inner cylinder, and it depend on the material. For the shear rate factor, the independence of the shear rate holds only for linear viscoelastic materials or Newtonian fluids [25]. For a concentric cylinder geometry, the corresponding shear rate factor can be expressed as shown in equation (4.3) [25].

$$F_{\dot{\gamma}} = \frac{2R_2^2}{R_2^2 - R_1^2} \tag{4.3}$$

Where R_2 is the outer cylinder radius $[m]$.

For Newtonian fluids, equation (4.2) and equation (4.3) can be combined in order to express the viscosity, η $[Pa\ s]$, as a function of the rheometer outputs, torque and angular velocity, in addition to the dimensions of the geometry. Introducing equations for shear stress, equation (4.4), shear rate, equation (4.5), and viscosity, equation (4.6):

$$\sigma = F_\sigma \Gamma \tag{4.4}$$

$$\dot{\gamma} = F_{\dot{\gamma}} \Omega \tag{4.5}$$

$$\eta = \frac{\sigma}{\dot{\gamma}} \tag{4.6}$$

By combining equation (4.4) and 4.5 with equation (4.6), and putting in expressions for the shear stress and shear rate factors, the viscosity can be expressed solely by dimensions of the setup in addition to the outputs from the rheometer experiments, as seen in equation (4.7).

$$\frac{\Gamma}{\Omega} = \eta \frac{4\pi R_1^2 R_2^2}{R_2^2 - R_1^2} h \tag{4.7}$$

For the purpose of determining the dimensions of the geometry, and separating the effective height from the effective radius, the immersed height, h, is broken up into two terms, as seen in equation (4.8).

$$h = H - y \tag{4.8}$$

Where H is the effective height of the geometry $[m]$, and y is the nonwetted height $[m]$. In addition, a friction coefficient, C, can be introduced to represent the internal equipment resistance, as well as the resistance to rotating in the air without any sample $[Nms]$[25]. By introducing equation (4.8) and the friction coefficient, the viscosity, and effective dimensions are related, as shown in equation (4.9).

$$\frac{\Gamma}{\Omega} - C = \eta \frac{4\pi R_1^2 R_2^2}{R_2^2 - R_1^2} (H - y) \tag{4.9}$$

The determination of the effective height, H, involves experimentation with various Newtonian fluids at different nonwetted heights, y, while measuring the required torque at predetermined angular velocities. In order to obtain the effective height, H, both sides of equation (4.9) are divided by the viscosity, and the resulting values are plotted on the y-axis as a function of nonwetted height, y, on the x-axis. Extrapolation to the x-axis allows for the determination of the effective height, at which point the torque reading is equal to the friction coefficient, C, indicating that the full vane is above the sample. It should be noted that this methodology is only applicable to Newtonian fluids, as the viscosity must be constant and known for all angular velocities.

An observed linear relationship for pairs of angular velocity and torque demonstrates the correspondence between a vane geometry and a concentric cylinder. The lack of dependence on the angular velocity shows a negligible contribution of fluid circulation between the blades of the vane[25].

4.5.4 Vane geometry with non-Newtonian fluids

When the effective dimensions of a given vane have been determined, the vane may be utilized when testing fluids with non-Newtonian behavior. The shear rate factor and shear stress factors vary in the gap between the vane blades

and container wall, and correction is necessary to include this alteration [28]. A standard gap correction for the shear stress factor and shear rate factor takes into account the averaged geometric size and can be seen in equation (4.10) and (4.11), respectively [25].

$$\overline{F_\sigma} = \frac{R_1^2 + R_2^2}{4\pi R_1^2 R_2^2 h} \tag{4.10}$$

$$\overline{F_{\dot{\gamma}}} = \frac{R_1^2 + R_2^2}{R_2^2 - R_1^2} \tag{4.11}$$

These factors can be utilized in conjunction with the measured angular velocity and torque to compute the shear rate and shear stress, correspondingly. The apparent viscosity can subsequently be determined for each pair by dividing the shear stress by the shear rate.

An alternative approach to the correction step involves the utilization of shear rate and shear stress factors for Newtonian fluids, as presented in equation (4.2) and equation (4.3). Due to the varying shear rate and stress, a correction needs to be applied to the viscosity. The resulting corrected viscosity is seen in equation (4.12) [25] [31].

$$\eta_{\text{corrected}} = \frac{\eta_{\text{apparent}}}{1 + C_R} \tag{4.12}$$

Where $\eta_{\text{corrected}}$ is the corrected viscosity $[Pa\ s]$, η_{apparent} is the apparent viscosity from the measured angular velocity and torque $[Pa\ s]$, and C_R is a correction factor $[-]$. The correction factor, C_R, is approximated by the following power series, showed in equation (4.13), (4.14), and (4.15) [25]:

$$C_R = \frac{s^2 - 1}{2s^2} \frac{s'}{ln(s)} [1 + \frac{2}{3} ln(s) + \frac{1}{3} s' - \frac{1}{45} s'^3 + \frac{2}{945} s'^5 - \frac{1}{4725} s'^7] \tag{4.13}$$

$$s' = -\frac{dln(\eta_{\text{apparent}})}{dln(\sigma_1)} ln(s) \tag{4.14}$$

$$s = \frac{R_2}{R_1} \tag{4.15}$$

4.5.5 Normal forces and Weissenberg effect

If a cylindrical rod is rotated steadily in a container filled with a Newtonian liquid, the surface near the rod is depressed due to the inertial forces created by the rotation. However, in the case of a non-Newtonian liquid with measurable normal stress, the free surface can exhibit a remarkable rise. This is due to the

tension in the direction of flow, which generates an inward pressure that increases as one approaches the axis of rotation. The pressure can be sufficiently high to counteract the centrifugal force effects, resulting in the upward movement of the liquid around the rod[32]. As a consequence, the liquid is drawn towards the rod and rises up around it, instead of being thrown outwards.

A sample that is drawn towards the vane and rod, and rises up around it, may induce alternations in the resistance on the vane, resulting in non-consistent results which again leads to lower reproducibility. The Weissenberg effect can be seen in figure 4.3, from an experiment conducted on Exilva.

Figure 4.3: Illustration of the Weissenberg effect. The picture is from an experiment conducted on Exilva with a concentration of 3.60% with a V40/20 vane. It is clearly seen that the material is drawn upwards around the vane shaft, resulting in an alternated resistance to flow.

4.6 Fluid flow types

The type of fluid flow occurring in pipes is important when looking at fluid dynamics. For fluids moving through closed systems, two distinct flow types can be observed. Dependent on the conditions, the flow is either laminar or turbulent[33].

Generally, laminar flow is a smooth flow at low velocities, where the fluid particles slide by each other in order, without forming swirls. Turbulent flow is a disturbed and uneven flow occurring at higher velocities. Reynolds number can be utilized to estimate which flow type will occur at given conditions[33].

4.6.1 Reynolds number

The transition from laminar flow to turbulent flow is a function of not only flow velocity but also the density and viscosity of the fluid, in addition to the diameter of the pipe where the flow is occurring[34]. This relationship is combined into an equation for the Reynolds number, as seen in equation (4.16).

$$N_{Re} = \frac{D\nu\rho}{\mu} \tag{4.16}$$

Where N_{Re} is the Reynolds number $[-]$, D is the diameter of the pipe $[m]$, ν is the average velocity of the fluid in the pipe $[m/s]$, ρ is the density of the fluid $[kg/m^3]$, and μ is the fluid viscosity $[Pa\ s]$[33]. Reynolds number is a quick and easy way to estimate which type of flow is to be expected. For a straight circular pipe, values of the Reynolds number below 2100 ($N_{Re} < 2100$) result in laminar flow, and values above 4000 ($N_{Re} > 4000$) result in a turbulent flow. For values between the two ($2100 < N_{Re} < 4000$), the flow is in a transition region. Within the transition region, the flow may either be laminar or turbulent, meaning it won't be predicted easily[33].

4.6.2 Laminar flow

Laminar flow, also called streamline or viscous flow, is a type of fluid flow in which the fluid particles move in a smooth manner along the direction of flow[34]. The liquid flows in parallel layers that do not form any types of eddies or vortices, and thus the liquid is not mixed. For flow in pipes, laminar flow generally occurs when the liquid has a high viscosity and the flow velocity is low[33].

For laminar flow, the velocity of the liquid particles varies along the radius of the pipe cross-section[34]. The particles at the pipe wall are at rest and have a velocity of zero, while the particles in the center of the pipe have the highest velocity. This leads to a parabolic relationship between the flow velocity and the distance to the pipe wall[35]. A flow velocity profile for laminar flow can be seen in figure 4.4.

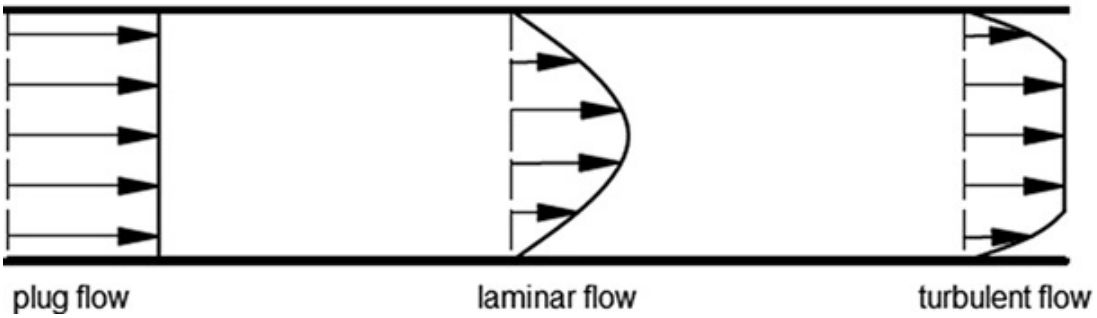

Figure 4.4: Velocity profiles of ideal plug flow, laminar flow, and turbulent flow[36]. The figure shows a pipe and the velocity profiles for each type of flow.

4.6.3 Turbulent flow

Turbulent flow is characterized by the irregular and chaotic movement of fluid particles. In contrast to laminar flow, in turbulent flow eddies and vortices are formed, causing fluctuations in flow velocity and pressure[33]. This causes

particles to mix well. For flow in pipes, turbulent flow occurs when the liquid has a low viscosity and the flow velocity is high[34].

The liquid velocity for turbulent flow varies along the radius of the pipe cross-section[34]. The velocity profile of turbulent flow is generally characterized by a flatter shape compared to the parabolic shape of the velocity profile in laminar flow. For turbulent flow, the velocity of fluid particles varies greatly, resulting in a highly irregular velocity distribution across the flow[37]. A flow velocity profile for turbulent flow can be seen in figure 4.4.

4.6.4 Plug flow

Plug flow is an ideal type of flow in which the fluid particles moves with minimal mixing and diffusion in the radial direction. The fluid particles move in a "plug" shape with the same velocity throughout. A flow velocity profile for a plug flow can be seen in figure 4.4.

Plug flow is found in combination with an annular flow. In the presence of yield stress, the central region of a fluid undergoes solid-like displacement, behaving as a plug[38]. The solid plug does not undergo shearing, and it is therefore treated as a solid body that moves along in the center of the pipe[39]. The geometry of plug flow can be seen in figure 4.5.

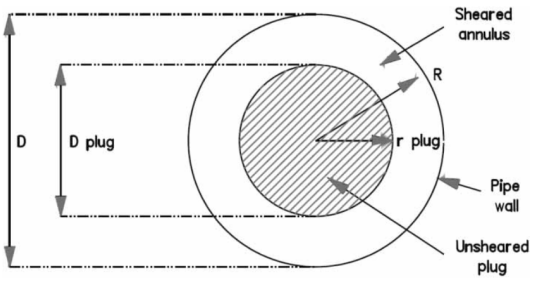

Figure 4.5: Geometry of plug flow. The figure is from Eshtiaghi, Markis & Slatter[39].

Given the center of the flow is now considered a solid plug, it is no longer being treated as part of the fluid flow. New methods have to be used in order to predict the flow behavior when only the outer annulus is considered to be flowing. A new technique, specially developed for non-Newtonian viscoelastic fluids, includes calculating the Reynolds number based on the flow velocity of the annulus and the size of the plug. The suggested revised Reynolds number can be seen in equation (4.17)[39].

$$N_{Re_3} = \frac{8\rho V_{ann}^2}{\tau_y + K(8V_{ann}/D_{shear})^n} \tag{4.17}$$

Where V_{ann} is the average flow velocity in the annulus $[m/s]$, τ_y is the yield stress $[Pa]$, K is the flow consistency index $[Pa\ s^n]$, and D_{shear} is the thickness of the sheared zone $[m]$. The diameter of the sheared zone is used as the characteristic

distance, as this is the only zone that is sheared when considering a plug flow. The diameter of the sheared zone can be calculated as shown in equation (4.18), (4.19), and (4.20).

$$D_{shear} = D - D_{plug} \tag{4.18}$$

$$D_{plug} = 2r_{plug} \tag{4.19}$$

$$r_{plug} = \frac{\tau_y}{\tau_0} R \tag{4.20}$$

Where τ_0 is the shear stress at the wall $[Pa]$. The diameter of the pipe, D, the diameter of the plug, D_{plug}, and the radius of the plug, r_{plug}, are visualized in figure 4.5. The average flow velocity in the annulus, V_{ann}, is calculated as shown in equation (4.21), (4.22), (4.23), and (4.24) [39].

$$V_{ann} = \frac{Q_{ann}}{A_{ann}} = \frac{Q - Q_{plug}}{\pi(R^2 - r_{plug}^2)} \tag{4.21}$$

$$Q_{ann} = u_{plug} A_{plug} \tag{4.22}$$

$$A_{plug} = \pi r_{plug}^2 \tag{4.23}$$

$$u_{plug} = \frac{D}{2K^{(1/n)}\tau_0} \frac{n}{n+1} [(\tau_0 - \tau_y)^{(n+1)/n}] \tag{4.24}$$

Where Q_{ann} is the volumetric flow rate in the annulus $[m^3/s]$, A_{ann} is the area cross-sectional area of the annulus $[m^2]$, u_{plug} is the plug velocity $[m/s]$, and n is the flow index $[-]$.

4.7 Fluid flow parameters

Fluid flow refers to the bulk motion of fluids, liquids, and gasses, as they traverse pipes, channels, and other conduits. Many parameters, both intensive and extensive, are to be considered when describing fluid flow systems. In fluid dynamics, extensive parameters are those that depend on the amount of fluid, while intensive parameters are those that do not depend on the quantity. It is however important to note that the nature of some extensive and intensive parameters may depend on the specific context and situation.

In addition to the obvious parameters such as the flow rate, both mass flow and volume flow, pipe size, and the dependent flow velocity, many fluid-dependent

intensive parameters need to be thoroughly described in order to analyze a fluid-flowing system.

4.7.1 Pressure difference and fluid movement

To induce motion in fluids, a driving force is necessary. The driving force may be either internal, such as temperature difference or concentration gradients, or external, such as pumps or gravity [33]. The rate of a transfer process is generally the ratio between the driving force and the resistance to flow. This relationship is shown in equation (4.25) [33].

$$\text{Rate of transfer} = \frac{\text{driving force}}{\text{resistance}} \tag{4.25}$$

In fluid mechanics, the driving force is related to the pressure difference between two points in a fluid-flowing system. When a pressure difference is present, the fluid flows from the higher pressure zone to the lower pressure zone. The pressure difference creates a force that drives the fluid flow, and the extent of this force is proportional to the pressure difference. Usually, the pressure drop is induced by a mechanical device, such as a pump, to increase the mechanical energy of the fluid, which in return increase the velocity of the fluid flow [40].

4.7.2 Fluid friction and pressure loss

In a closed system, the movement of fluids is impeded by frictional forces, which arise from the fluid's resistance to flow, and result in a pressure loss [33]. The main determinants of a fluid's resistance to flow are fluid velocity and fluid viscosity. The resistance to flow is proportional to both velocity and viscosity. In addition, other factors such as pipe length, pipe roughness, and bends and valves, also increase the frictional forces [40].

For Newtonian fluids in laminar flow, the pressure drop due to friction can be described by the Hagen-Poiseuille equation, as seen in equation (4.26) [33].

$$\Delta p_f = (p_1 - p_2)_f = \frac{32\mu\nu(L_2 - L_1)}{D^2} \tag{4.26}$$

Where p_1 is the pressure at point 1 $[Pa]$, p_2 is the pressure at point 2 $[Pa]$, μ is the apparent viscosity $[Pa\ s]$, ν is the average velocity in the tube $[m/s]$, $(L_2 - L_1)$ is the length of the tube from point 1 to point 2 $[m]$, and D is the diameter of the pipe $[m]$. The Hagen-Poiseuille equation is useful for determining the viscosity of Newtonian fluids, by measuring the pressure drop and flow rate for a pipe with known length and diameter. The total mechanical energy loss due to friction can be calculated as shown in equation (4.27) [33].

$$F_f = \frac{(p_1 - p_2)_f}{\rho} = \frac{\Delta p_f}{\rho} \tag{4.27}$$

Where ρ is the density of the fluid $[kg/m^3]$. Equation 4.27 only holds for fluids with constant density.

4.7.3 Fanning friction factor

A common parameter used in fluid dynamics is the Fanning friction factor, f. It is defined as the ratio between the drag force per wetted surface area, which is equal to the shear stress at the pipe wall, and the local flow kinetic energy times fluid density. The force is equal to the pressure loss due to friction times the cross-sectional area of the pipe. Further, the area of the wetted area of the pipe is equal to the cross-sectional area times the length. The Fanning friction factor is calculated as shown in equation (4.28)[33].

$$f = \frac{\tau_s}{\frac{1}{2}\nu\rho} = \frac{(\Delta p_f \pi R^2)/(2\pi R \Delta L)}{\frac{1}{2}\nu^2\rho} = \frac{\Delta p_f R}{\nu^2 \rho \Delta L} \tag{4.28}$$

Where R is the radius of the pipe $[m]$. By introducing the pipe diameter, D, instead of the radius, and rearranging the equation, the pressure loss is isolated, as shown in equation (4.29).

$$\Delta p_f = 4f\rho\frac{\Delta L}{D}\frac{\nu^2}{2} \tag{4.29}$$

Combining equation (4.27) and 4.29 leads to the mechanical energy loss due to friction as a function of the Fanning friction factor, fluid flow velocity, and pipe dimensions, as seen in equation (4.30).

$$F_f = \frac{\Delta p_f}{\rho} = 4f\frac{\Delta L}{D}\frac{\nu^2}{2} \tag{4.30}$$

Further, for laminar flow only, equation (4.26) and 4.29 can be combined to show a relationship between the Fanning friction factor and Reynolds number. The derivation of the relationship is shown in equation (4.31), (4.32), and (4.33).

$$\Delta p_f = \frac{32\mu\nu(L_2 - L_1)}{D^2} = 4f\rho\frac{\Delta L}{D}\frac{\nu^2}{2} \tag{4.31}$$

$$16 = f\frac{D\nu\rho}{\mu} = fN_{Re} \tag{4.32}$$

$$f = \frac{16}{N_{Re}} \tag{4.33}$$

This ratio holds strictly for laminar flow, which is when the Reynolds number is below 2100[33].

For turbulent flow, the friction factor is dependent on the Reynolds number, much like for laminar flow[33]. However, for turbulent flow, the Fanning friction factor has to be determined empirically, rather than theoretically. If the friction loss is already set from the available head of the liquid, together with the known dimensions of a pipe, it is the fluid flow velocity that needs to be calculated. The velocity appears in both the relationship for the Reynolds number, equation (4.16), and the relationship for the Fanning friction factor, equation (4.28). This implies that the solution for the velocity only can be obtained through a process of successive approximations through iterations and experimentation[33].

4.7.4 Shear rate in pipes

The shear rate in pipes generally refers to the rate at which layers of the fluid move pass each other when the bulk fluid moves through a pipe. The shear rate is caused by the friction between the pipe wall and the fluid[41]. This results in a velocity gradient across the cross-sectional area of the pipe, as seen for laminar flow, turbulent flow, and plug flow in figure 4.4. It is an important parameter when looking at fluid behavior, as it is impacted by fluid viscosity and fluid viscosity. In addition, it varies with the distance to the pipe wall[33].

4.7.5 Shear stress in pipes

Shear stress in pipes generally refers to the force per unit area that is exerted on a fluid, while it flows through the pipe. The force is due to the frictional forces between the moving fluid and the pipe wall. This force is tangential to the direction of fluid flow and is responsible for the deformation of the fluid layers within the flow. The extent of the shear stress is dependent on fluid viscosity, fluid velocity, and also to some extent, the roughness of the pipe. The shear stress is not constant, and it varies with the distance to the pipe wall[33].

4.8 Estimation of fluid flow parameters

Rheology models are employed to derive rheological parameters and characteristics, including but not limited to shear stress, yield stress, thixotropy, viscosity, and the critical point of transition between laminar and turbulent flow[39][3][8]. Multiple possible rheology models for non-Newtonian fluids, including Bingham, Herschel-Bulkley, and Ostwald-De Waele, are presented in the precursor of this thesis[1]. Prior empirical investigations indicate that the Herschel-Bulkley model is the most pertinent approach for this study[1].

4.8.1 Herschel-Bulkley model

The Herschel-Bulkley model, which accounts for the effect of yield stress, is expressed mathematically in equation (4.34), and is considered appropriate when the yield stress is too large to be ignored[3][42]. This model is suitable for analyzing the behavior of hydrolyzed sludge, digestate sludge, and a blend of the two

within the higher range of dry solid content of 5-15%[43].

$$\tau = \tau_0 + K\dot{\gamma}^n \tag{4.34}$$

Further, the Herschel-Bulkley model also works great in analyzing MFC suspensions, since this material follows the behavior of sludge to a great extent, as explained in section 4.3.

5 Materials

5.1 Rheometer

In conducting rotational rheometer testing, a Brookfield *R/S plus SST2000 Soft Solid Tester* rheometer was utilized, along with three different vanes. A V10/5 vane (with dimensions of length 10 mm and diameter 5 mm), a V40/20 vane (with dimensions of length 40 mm and diameter 20 mm), and a V80/40 vane (with dimensions of length 80 mm and diameter 40 mm)[44]. PVC pipes and lids were used as containers for the material, with dimensions of 12 cm in height and 48 mm in diameter. Additional experiments were run with a larger container, a glass beaker with dimensions of 14.5 cm in height and 100 mm in diameter. The containers together with respective alias are shown in table 5.1. Control and data recording were performed via Brookfield's Rheo3000 software, operated from a personal computer. To ensure accurate results, measurements were maintained within the recommended torque range of 1.5-50 mNm, as specified by Brookfield.

Complementary rheometer measurements were conducted with a Kinexus ultra+ Rheometer from NETZSCH-Gerätebau GmbH, using the rSpace software to control and record data. A cone-plate geometry (CP40/4, with a diameter of 40 mm and a cone angle of 4° over a plate with a diameter of 40 mm) was employed as the geometry for these measurements.

Table 5.1: Dimensions of containers used in experiments on determining effective radius and effective height of vanes. The containers are referred to as small and large.

Container	Alias	Height [cm]	diameter [cm]
PVC pipe	Small container	12	4.8
Glass beaker, 1L	Large container	14.5	10

5.2 Pipe rig

The pipe rig testing facility was housed within a thermally insulated container measuring 40 feet in length. The configuration involved the utilization of two pipes with diameters of 2.88 cm and 5.5 cm. One end of the pipes was connected to a pump, while the other end extended over a bucket placed on a weighing scale. The pipes were installed at a gradient of 3 degrees to facilitate easier cleaning and drainage after conducting experiments.

Pressure and temperature sensors were strategically positioned in the test pipe to gather data for analysis. At both ends of the pipe, pressure sensors were installed, offering flexibility in their placement. The sensors could be adjusted to distances of 0.8, 2.8, or 4.8 meters from each other, allowing for precise measurements at specific locations. Furthermore, temperature sensors were placed outward from each pressure sensor, precisely 10 cm away. This arrangement facilitated the logging of temperature measurements, providing a comprehensive profile of temperature distribution along the entire length of the pipe.

To accommodate experiments involving fluids with different viscosities and flow velocities, two distinct types of pumps were installed. A MONO centrifugal pump was installed for less viscous materials, while a MONO eccentric screw pump was employed for more viscous substances. However, for this project, only the eccentric screw pump was used. The pumps were installed at ground level, with the starting point of the pipes positioned 1.75 meters above the ground. Consequently, the material being tested had to be pumped to an elevation of 1.75 meters before entering the section of the pipe containing the sensors.

Data captured by the two pressure sensors, two temperature sensors, and the weighing scale were collected using a programmable logic controller (PLC) at a frequency of two readings per second. The collected data was then exported to a connected computer for further analysis and processing. An illustration of the pipe rig setup can be seen in figure 5.1.

(a) Scale for measuring flow rate. **(b)** Pipes and setup. **(c)** Pump hopper.

Figure 5.1: Illustration of the pipe testing rig. The setup consisted of a pump hopper to fill the material, multiple pipes of different diameters and lengths, and a scale to record mass flow.

5.3 Model fluid - Exilva

Three batches of Exilva samples were obtained from Borregaard, each with different concentrations of 2%, 2.43%, and 3.55%, respectively. Borregaard provided these concentrations, and the dry solids contents were validated through an independent method. The validation involved heating samples of each concentration at 105℃ for a duration of one night and measuring the remaining dry solids. The measured concentrations were found to be 1.86%, 2.44%, and 3.60%. The industrial material with the lowest concentration had the maximum deviation from the stated concentration, which is a reasonable observation, as it is the most frequently produced industrial material, and such industrial processes may induce variations. The measurements are documented in appendix C.

The densities of the Exivla samples were tested for use in subsequent calculations.

It was discovered that all the densities were nearly equal to that of water, and for all practical purposes, the densities were assumed to be the same as that of water, i.e. 1 kg/L. The measurements are documented in appendix C. All samples were kept at a stable room temperature of 21℃. Table 5.2 provides an overview of all the samples.

Table 5.2: Samples and their amount of dry solids and density.

Sample	**DS %** $[g/g]$	**Density** $[kg/L]$
Exilva F	1.86	1.00
Exilva F	2.44	1.00
Exilva F	3.60	1.01

5.4 Other Newtonian fluids

The investigation involved conducting experiments on multiple Newtonian fluids with consistent and measurable viscosity properties. A 99.9% glycerol solution was selected due to the well-documented data available in the literature. Furthermore, Eldorado dark syrup, known for its high viscosity as a Newtonian fluid, was also tested. The syrup was further diluted to a weight percentage of 90%. The viscosities of these fluids are presented in table 5.3. While some viscosity values were sourced from literature, measurements were performed using the Kinexus ultra+ Rheometer for fluids without readily available data, and the results are considered table values in this thesis.

Table 5.3: Newtonian fluids and measured viscosities.

Material	**Viscosity** $[Pa\ s]$
Eldorado dark syryp	59.83
Eldorado dark syryp 90%	1.661
Glycerol 99.9%	1.216

6 Method

6.1 Preparation of samples - Rheometer

Exilva exhibits a consistency that is analogous to toothpaste. The transfer of samples from storage containers to test containers was accomplished by employing a metal spoon/spatula. To prevent the development of air pockets in the test containers during sample transfer, gentle tapping of the test container on the table was performed to encourage the settling of the sample. Tapping also facilitated an even distribution of the material in the container. The test containers were filled with a volume of approximately 170-180 mL samples.

The rheometer used in the study was fitted with three clamps to hold the test container securely in place. To ensure consistent and stable conditions, with the vane positioned uniformly, two of the clamps were kept immobile throughout the testing period. The third clamp was loosened and adjusted only for the purpose of placing and removing test containers. After the placement of the test container, the last clamp was secured, and the vane was immersed to the required depth.

6.1.1 Angular velocity sweep

To establish a dependable range for the controlled angular velocity tests, an angular velocity sweep was performed on each sample. The process involved executing a step-wise increase of torque from minimum to maximum, while simultaneously recording the corresponding angular velocities. Following the angular velocity sweep, the controlled angular velocity test was updated to encompass the minimum and maximum angular velocities that were deemed reliable. This was implemented to ensure that both tests were executed within the reliable range while avoiding exceeding the limits of the instrument, which would lead to an unsuccessful test and loss of valuable data.

6.1.2 Internal equipment resistance

The internal equipment resistance, the friction coefficient, C, was measured by running a program in air, without a sample. The program was run for all vanes at many different angular velocities to check for velocity dependence. No torque readings were obtained, meaning that the equipment had no internal resistance, and the coefficient was assumed to be zero.

6.2 Effective dimensions - Newtonian fluids

The vanes were immersed in different submergence depths and rotated at varying angular velocities. The experimental setup was employed to examine multiple Newtonian fluids exhibiting distinct viscosities. Each angular velocity was held constant for 60 seconds, for the torque readings to stabilize. Every experiment

was started at the lowest angular velocity and raised step-wise for every minute. An example of a test program can be seen in appendix A.

Table 6.1, table 6.2, and table 6.3 show the different depths and angular velocities employed for each vane. Every angular velocity was employed for every non-wetted height.

Table 6.1: Test materials, non-wetted heights, and angular velocities for the V80/40 vane.

Material	**Non-wetted height** $[cm]$	**Angular velocities** $[s^{-1}]$
Glycerol 99.9%	3, 1, 0, -1, -3	5, 10, 15, 20
Syrup 100%	3, 1, 0, -1, -3	0.2, 0.4, 0.6, 0.8
Syryp 90%	6.5, 5, 3, 1, 0, -1	5, 10, 15, 20

Table 6.2: Test materials, non-wetted heights, and angular velocities for the V40/20 vane.

Material	**Non-wetted height** $[cm]$	**Angular velocities** $[s^{-1}]$
Glycerol 99.9%	2, 1, 0, -1, -3	30, 40, 50, 60
Syrup 100%	3, 2, 1, 0, -1	2, 4, 6, 8
Syryp 90%	3, 2, 1, 0, -1	30, 40, 50, 60

Table 6.3: Test materials, non-wetted heights, and angular velocities for the V10/5 vane.

Material	**Non-wetted height** $[cm]$	**Angular velocities** $[s^{-1}]$
Syrup 100%	0.6, 0.3, 0, -0.3	30, 40, 50, 60

6.2.1 Test of effective dimensions

In order to verify the applicability of equation (4.9) for viscosity estimation, and the assess the usability of the estimated effective height and radius, experimental investigations were conducted using a material with a known viscosity. A 90% syrup solution was prepared by diluting a 100% syrup solution, and its viscosity was determined using the Kinexus Ultra+ Rheometer. Subsequently, the effective dimensions were determined, and the viscosity of the 90% syrup solution was measured using the Brookfield rheometer, at different submersion heights.

6.3 Effective dimensions - non-Newtonian fluids

6.3.1 Controlled angular velocity

The experimental procedure involved conducting controlled angular velocity tests referred to as Ramp tests in Rheo3000. These tests entailed systematically varying the angular velocity from low to high and then returning it to a low value, each step being executed at a predetermined rate. The torque was measured as the dependent variable, resulting in pairs of angular velocity and torque values. Considering the varying viscosities of the samples, certain samples were subjected to a wider range of angular velocities. The angular velocity range was

optimized within the constraints of the rheometer's reliable torque range and reliable angular velocity range. To ensure robustness, controlled angular velocity tests were performed in triplets, and the average of the three runs was taken as the final result. The detailed program for executing the controlled angular velocity tests can be found in appendix A.

6.3.2 Determination of proper ramp length

The material exhibited a pronounced sensitivity to the incremental rate at which the angular velocity was increased. In order to mitigate this effect and obtain reliable data, a series of experiments were performed wherein the angular velocity was increased at various rates. The ramp-up time, corresponding to the duration of the velocity increment, was progressively extended until reaching a point where no additional impact on the material's response was observed upon further elongation of the ramp-up time.

6.4 Commissioning of the pipe rig testing facility

The commissioning process of the pipe rig testing facility involved a series of steps to ensure the proper functioning and accuracy of the equipment. However, during the commissioning phase, several challenges were encountered, including leakages in the connections between pipe sections, a pump that pumped in the wrong direction, and incorrectly connected pressure and temperature sensors in the electrical cabinet, leading to incorrect data readings on the PLC. These issues required early identification and resolution to achieve reliable and accurate experimental results.

To begin the commissioning process, the physical setup of the pipe rig was inspected to verify the correct installation in the thermally insulated container, the pipes of varying diameters (2.88 cm and 5.5 cm), and the associated equipment. Attention was given to ensuring proper alignment, secure connections, and appropriate positioning of the pumps, pressure sensors, temperature sensors, and the weighing scale.

Addressing the first issue, leakages in the connections between pipe sections, a thorough examination of the joints and fittings was conducted. Each connection was carefully inspected, and any loose connections were identified and tightened as necessary. Special attention was paid to the sealing mechanism of the connections to prevent any potential leakages that could compromise the pressure and or flow rate readings.

Another issue revolved around incorrectly connected pressure and temperature sensors in the electrical cabinet, resulting in incorrect data readings on the PLC. The electrical connections of the sensors were carefully reviewed, and any incorrect wiring or misalignment was rectified. The proper functioning of the sensors was verified by detaching the sensors and applying pressure by hand to the

pressure sensors and heating by hand to the temperature sensors until correct measurements were achieved.

Another significant challenge encountered during the commissioning of the pipe rig testing facility was the need for proper ventilation of the pipe system to obtain consistent and reliable results. The presence of air pockets or trapped gases within the pipes could potentially interfere with the flow dynamics and disrupt the accuracy of the experimental measurements. Test runs showed that proper ventilation had to be executed both upstream and downstream in order to obtain reliable results.

Once the identified problems were resolved, the commissioning process continued by initiating a series of test runs to ensure the overall functionality and reliability of the pipe rig testing facility. These test runs involved operating the pumps and monitoring the readings from the pressure sensors, temperature sensors, and weighing scale.

In conclusion, the commissioning of the pipe rig testing facility was a comprehensive and precise process. Despite the challenges faced, including leakages in pipe connections, a pump malfunction, and incorrectly connected sensors, each issue was promptly identified and rectified. The successful commissioning ensured the reliability and accuracy of the experimental setup, allowing for precise data collection and analysis in subsequent experiments and research activities.

6.5 Preparation of samples - Pipe rig

The material was stored in large blue barrels (120L) and smaller white buckets (25L). Before the material was poured into the hopper of the pump, it was gently mixed in order to combine water and material which had separated during storage.

6.5.1 Pipe rig experiments

Experiments were carried out for all three concentrations of Exilva. Nine motor speeds were used, varying from 10 to 50 Hz, corresponding to the minimum and maximum allowable pump speed for the eccentric screw pump. A summary of the experiments is shown in table 5.2. The centrifugal pump was not used for any experiments in this thesis.

When the hopper of the pump was filled with material, the pump was initiated at a predetermined velocity. In order to release any potentially trapped air from the system, a valve was opened both upstream and downstream of the pressure sensors to facilitate ventilation of the pipes. Subsequently, the pump was allowed to operate for 20 seconds to establish a stable flow rate prior to commencing measurements. Each flow rate was maintained for a duration of 1 minute, during which the pressure and temperature were recorded. After 1 minute had elapsed, the pump speed was adjusted to the next predetermined

value, and a 20-second interval was observed to ensure the new flow rate reached stability before conducting measurements at the new speed. The purpose of the 20-second wait time was to enable the flow rate to stabilize before data collection.

Both the 2.88 cm and 5.5 cm pipes were used for the 2.44% and 3.60% concentrations. Due to a lower amount of 1.86% material, only the smaller 2.88 cm pipe was used for that concentration. Further, two different pipe lengths, 2.78 meters, and 4.79 meters, were used. A summary of the experiments can be seen in table 6.4.

Table 6.4: Pipe sizes and pump speeds used for each concentration of Exilva.

Material	**D [cm]**	**L [m]**	**Pump speed [Hz]**
Exilva 1.86%	2.88	2.78, 4.79	10, 15, 20, 25, 30, 35, 40, 45, 50
Exilva 2.44%	2.88, 5.5	2.78, 4.79	10, 15, 20, 25, 30, 35, 40, 45, 50
Exilva 3.60%	2.88, 5.5	2.78, 4.79	10, 15, 20, 25, 30, 35, 40, 45, 50

7 Results - Rheometer

7.1 Vane effective dimensions - Newtonian fluid

In conjunction with known viscosity values, all angular velocity and torque pairs were utilized to calculate $(\Gamma/\Omega - C)/\eta$ using equation (4.9). These calculated values were plotted against the non-wetted height, y, to demonstrate the relationship between flow resistance and the non-wetted height. Linear regressions were conducted, and extrapolations were made to $(\Gamma/\Omega - C)/\eta = 0$, meaning y=H, in order to determine the effective height of the vane. The effective radius was subsequently obtained from equation (4.9).

The linear regression analysis solely considered values when the non-wetted height was above zero, as the linear relationship does not extend beyond this range. When the vane is fully submerged, the resistance continues to increase with further submersion; however, this is attributable to resistance originating from the vane shaft rather than the vane itself. The ensuing sections present the results pertaining to the effective height and radius of three vane sizes with varying dimensions.

7.1.1 V80/40

Figure 7.1 presents the results of the conducted linear regressions for the V80/40 vane. Panel a) illustrates the experimental data obtained from the small container, while panel b) displays the experimental data from the large container. The effective height and radius values, along with their corresponding computed standard deviations, can be found in table 7.1.

Comparing the two containers, it is observed that the effective radius exhibits close agreement, differing by only 0.04 cm, corresponding to a relative increase of 2.2% in the effective height when transitioning from the small to the large container. However, there is a more pronounced variation in the effective height, with a discrepancy of 0.65 cm between the small and large containers. This discrepancy corresponds to a relative increase of 7.1% in the effective height when transitioning from the small to the large container.

Table 7.1: Effective radius and effective height of the V80/40 vane, computed for each container separately.

	Small container	**Large container**
Effective radius, R_1 $[cm]$	1.78	1.82
R_1 std $[cm]$	0.05	0.07
Effective height, H $[cm]$	8.51	9.16
H std $[cm]$	0.01	0.01

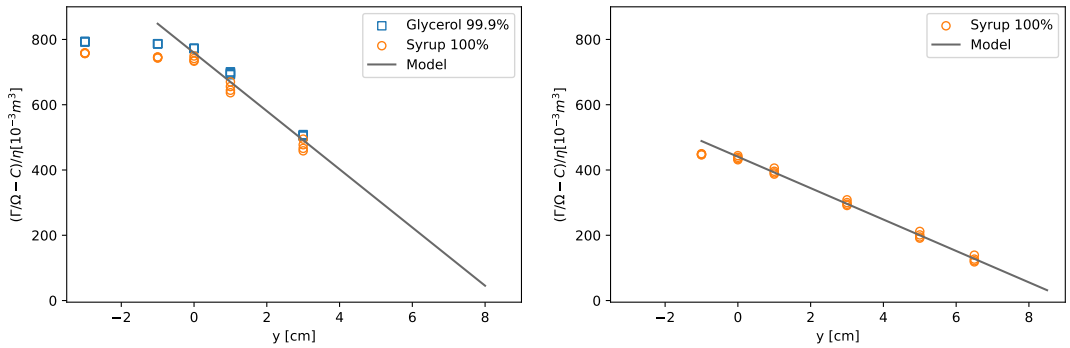

(a) Small container **(b)** Large container

Figure 7.1: $(\Gamma/\Omega - C)/\eta$ as a function of non-wetted length, y, for both the small container and the large container, for the V80/40 vane. This analysis aims to determine the effective height and radius of the vane. Each point represents a pair of torque and angular velocity measurements. The model represents equation (4.9).

7.1.2 V40/20

The outcome of the performed linear regressions for the V40/20 vane is demonstrated in figure 7.2. Panel a) exhibits the experimental data derived from the small container, whereas panel b) showcases the experimental data collected from the large container. Details concerning the effective height and radius, alongside their associated computed standard deviations, can be accessed in table 7.2.

In contrast to the V80/40 vane, the effective height of the V40/20 vane exhibits greater consistency across the two containers. The variation in effective height is merely 0.11 cm, resulting in a relative decrease of 2.7% in the effective height when transitioning from the small to the large container. Conversely, the disparity in effective radius is more significant, with a deviation of 0.09 cm. This corresponds to a relative increase of 10.3% in the effective radius when transitioning from the small to the large container.

Table 7.2: Effective radius and effective height of the V40/20 vane, computed for each container separately.

	Small container	**Large container**
Effective radius, R_1 $[cm]$	0.87	0.96
R_1 std $[cm]$	0.10	0.13
Effective height, H $[cm]$	4.18	4.07
H std $[cm]$	0.05	0.05

7.1.3 V10/5

Figure 7.3 illustrates the results obtained from the conducted linear regressions for the V10/5 vane. Panel a) presents the experimental data obtained from the small container, while panel b) displays the experimental data collected from the

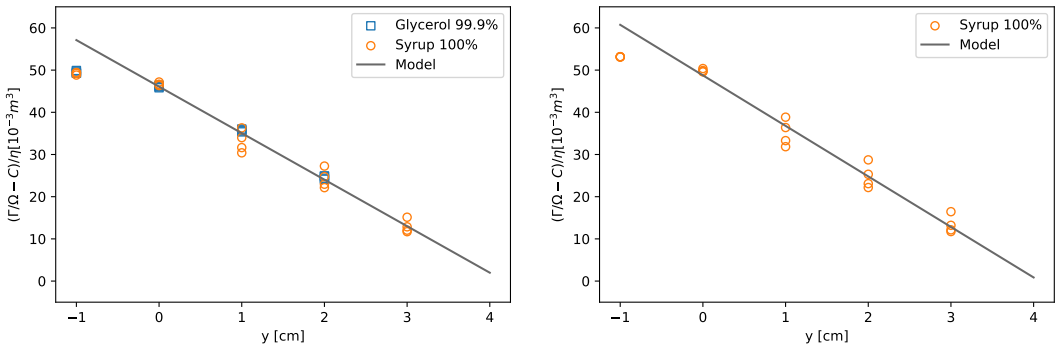

(a) Small container **(b)** Large container

Figure 7.2: $(\Gamma/\Omega - C)/\eta$ as a function of non-wetted length, y, for both the small container and the large container, for the V40/20 vane. This analysis aims to determine the effective height and radius of the vane. Each point represents a pair of torque and angular velocity measurements. The model represents equation (4.9).

large container. Comprehensive information regarding the effective height and radius, including their respective computed standard deviations, can be found in table 7.3. Because of the small size of the vane, only very viscous fluids gave consistent torque readings. This resulted in only the 100% syrup offering enough resistance to flow, and thus the vane was only tested in one fluid.

In the case of the V80/40 and V40/20 vanes, the obtained results demonstrated consistency and minimal deviations. However, contrasting these findings, the results for the V10/5 vane exhibited significantly larger variations. As a consequence, the standard deviation values surpassed the estimated effective height and radius values. Undoubtedly, this data showcases inherent limitations with respect to its reliability and accuracy. As the resistance was too low to yield torque values within the reliable region, no further experiments were conducted using the V10/5 vane.

Table 7.3: Effective radius and effective height of the V10/5 vane, computed for each container separately.

	Small container	**Large container**
Effective radius, R_1 $[cm]$	0.19	0.19
R_1 std $[cm]$	0.30	0.31
Effective height, H $[cm]$	1.24	1.37
H std $[cm]$	2.47	2.81

7.2 Estimated viscosity of 90% syrup

Utilizing the previously derived effective height and radius values, the viscosity of the 90% syrup solution was computed and compared against reference values. This analysis was performed separately for each container, employing distinct

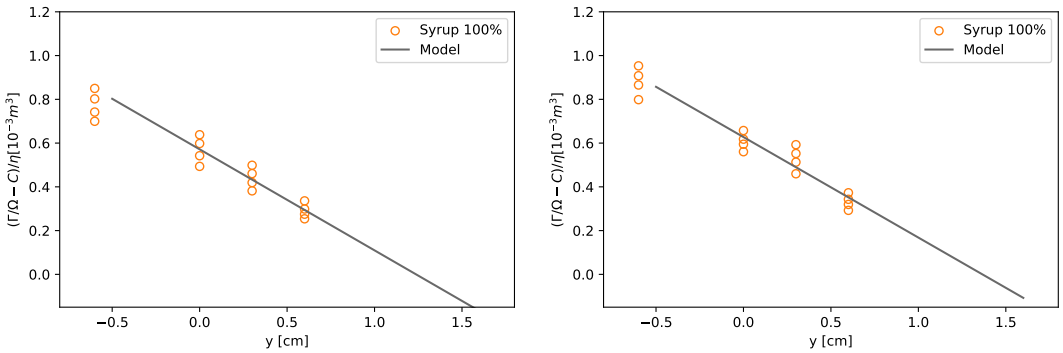

(a) Small container **(b)** Large container

Figure 7.3: $(\Gamma/\Omega - C)/\eta$ as a function of non-wetted length, y, for both the small container and the large container, for the V40/20 vane. This analysis aims to determine the effective height and radius of the vane. Each point represents a pair of torque and angular velocity measurements. The model represents equation (4.9).

effective height and radius values specific to each container. It is worth noting that viscosity estimations were exclusively carried out for the V80/40 and V40/20 vanes, considering the aforementioned difficulties and discrepancies encountered with the V10/5 vane.

7.2.1 V80/40

Table 7.4 presents the estimated viscosity values for the 90% syrup solution using the V80/40 vane at various submersion depths. To facilitate a comparison of container size and submersion depth, these results are visually depicted in figure 7.4.

Notably, the computed effective height and radius obtained from the small container yield a much more consistent viscosity estimation, with results that closely align with the reference values. Conversely, the large container consistently underestimates the viscosity across all submersion depths. It is noteworthy that both containers exhibit the lowest standard deviation at lower y-values, suggesting further experimentation should have the vane fully submerged in the sample (y=0).

7.2.2 V40/20

The estimated viscosity values for the 90% syrup solution utilizing the V40/20 vane at different submersion depths are provided in table 7.5. To enhance the analysis of container size and submersion depth, these outcomes are graphically represented in figure 7.5.

Similar to the V80/40 vane, the computed viscosity from the effective height and radius obtained from the small container yields much more consistent results when compared to the effective height and radius from the large container. In

Table 7.4: Estimated viscosity of 90% syrup for the V80/40 vane using the calculated effective dimensions for both containers separately.

	y=0cm	y=1cm	y=3cm	y=5cm	y=6.5cm
Small container					
Mean viscosity [Pa s]	1.62	1.64	1.65	1.62	1.62
std [Pa s]	0.04	0.04	0.06	0.09	0.17
Large container					
Mean viscosity [Pa s]	1.28	1.28	1.28	1.21	1.09
std [Pa s]	0.03	0.04	0.05	0.06	0.08

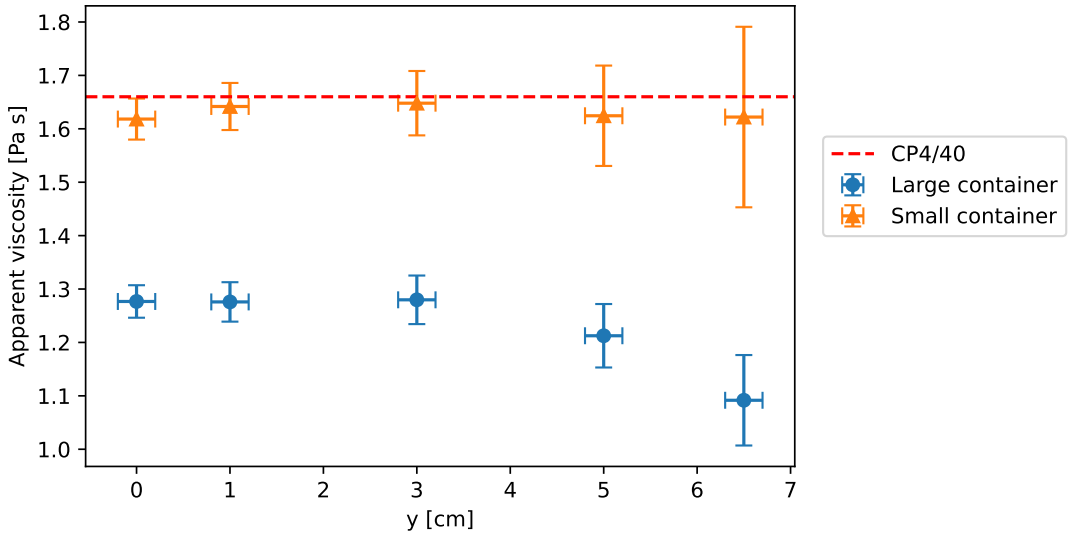

Figure 7.4: Estimated viscosity of 90% syrup using the previously calculated effective radius and height for the V80/40 vane. Estimations using the effective dimensions from both the small and large containers. The CP4/40 is the cone-plate geometry used as the table value.

addition, the viscosity estimations utilizing the small container are much more in conformity with reference values. As for the V80/40, the large container has a systematic deviation which underestimated the viscosity. It is noteworthy that both containers exhibit the lowest standard deviation at lower y-values, suggesting further experimentation should have the vane fully submerged in the sample (y=0).

7.3 Flow behavior of Exilva

Both the V80/40 and V40/20 vanes exhibit remarkable consistency across experiments and demonstrate adherence to reference values. However, due to its large size, the V80/40 vane may generate resistance and torque readings that exceed the reliable range of the rheometer. Past experimental observations with Exilva, a highly viscous fluid, revealed that the V80/40 vane is not suitable for such

Table 7.5: Estimated viscosity of 90% syrup for the V40/20 vane using the calculated effective dimensions for both containers separately.

	y=0cm	y=1cm	y=2cm	y=3cm
Small container				
Mean viscosity [Pa s]	1.64	1.70	1.76	1.78
std [Pa s]	0.09	0.12	0.18	0.36
Large container				
Mean viscosity [Pa s]	1.33	1.37	1.38	1.47
std [Pa s]	0.08	0.10	0.15	0.54

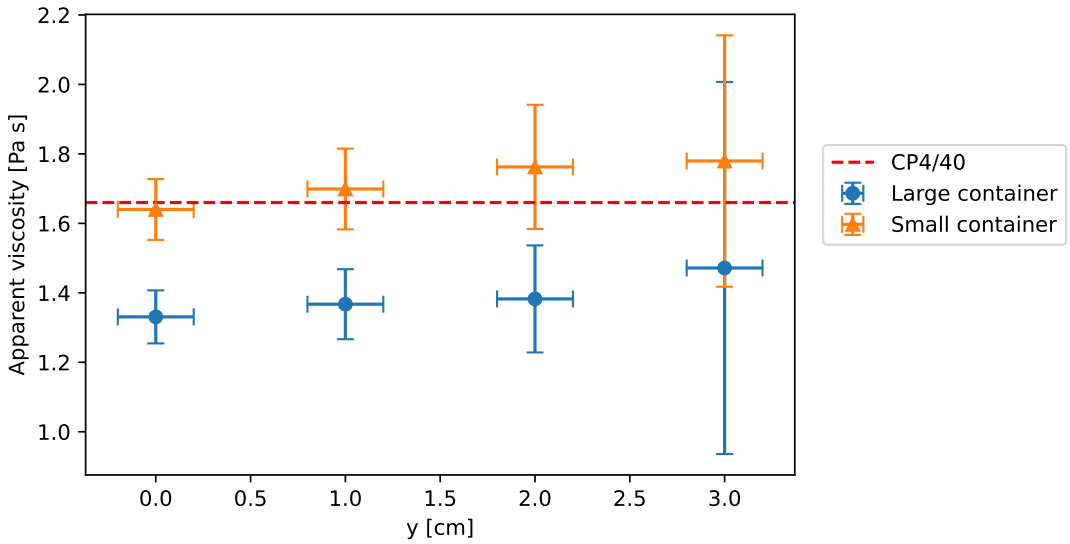

Figure 7.5: Estimated viscosity of 90% syrup using the previously calculated effective radius and height for the V40/20 vane. Estimations using the effective dimensions from both the small and large containers. The CP4/40 is the cone-plate geometry used as the table value.

fluids, particularly at concentrations exceeding 3%. Consequently, subsequent experiments involving Exilva exclusively employed the V40/20 vane.

7.3.1 Submersion of the vane to improve reproducibility

The experimental setup initially aimed for a vane depth of 0 cm within the fluid medium. Unfortunately, this approach resulted in significant noise and non-reproducibility, mainly thought to be attributed to the Weissenberg effect. The impact of this effect was particularly pronounced at higher concentrations and viscosities, intensifying the non-reproducibility challenges encountered during the experiments.

To address these issues, and to enhance the reproducibility of the experimental setup, an alternative approach was adopted. Instead of maintaining a vane depth

of 0 cm, the vane was submerged to a depth of y = -0.5 cm. This adjustment effectively mitigated the disadvantageous effects associated with the Weissenberg effect, resulting in improved reproducibility of the experimental outcomes.

By submerging the vane to a non-zero depth, the influence of the Weissenberg effect was significantly reduced, leading to less noise and enhanced reproducibility. The submerged vane created a more controlled environment for studying fluid behavior. It is important to acknowledge that submerging the vane to y = -0.5 cm introduced some additional resistance on the vane shaft. Nevertheless, this resistance was assumed to be negligible in the overall context of the experimental system. The advantages of improved stability and reproducibility outweighed any potential drawbacks of the additional resistance.

Following the decision to submerge the vane to a depth of y = -0.5 cm, the subsequent experimental investigations were conducted under this modified condition. Therefore, all discussions, interpretations, and conclusions presented in the following sections of this study are based on the experimental results obtained with the vane depth set at y = -0.5 cm.

7.3.2 ramp-up time dependency - slope

Curves were generated to examine the relationship between input angular velocity and output torque values for Exilva at three different concentrations: 1.86%, 2.44%, and 3.60%, for different ramp-up times. Each test was conducted by varying the angular velocity from 0.1 s^{-1} to 50 s^{-1} over a specified time period.

To ensure reproducibility, multiple ramp-up times were tested to identify the optimal slope that yielded consistent results. It should be noted that some noise and unexpected behavior were observed.

In figure 7.6, the flow curves for Exilva with a concentration of 1.86% are presented. The straight lines represent the input angular velocity, while the curved lines depict the corresponding output torque values. Overall, the results demonstrate a clear non-linear correlation between the applied angular velocity and the resulting torque, indicating the viscoelastic behavior of the system. Similar flow curves were obtained for Exilva at concentrations of 2.44%, figure 7.7, and 3.60%, figure 7.8.

For the 1.86% concentration, a ramp-up time of 5000 seconds was determined to be suitable for achieving a smooth transition from 0.1 s^{-1} to 50 s^{-1}. This duration allowed for the most reliable and reproducible results, minimizing any undesirable inconsistencies in the torque measurements.

Figure 7.7 illustrates the relationship between angular velocity, torque, and time for Exilva with a concentration of 2.44%. Similar to the 1.86% graph, the straight lines represent the input angular velocity, while the curved lines correspond to the output torque values. To ensure a seamless transition from 0.1 s^{-1} to 50 s^{-1}, a ramp-up time of 9000 seconds was determined to be optimal. This duration

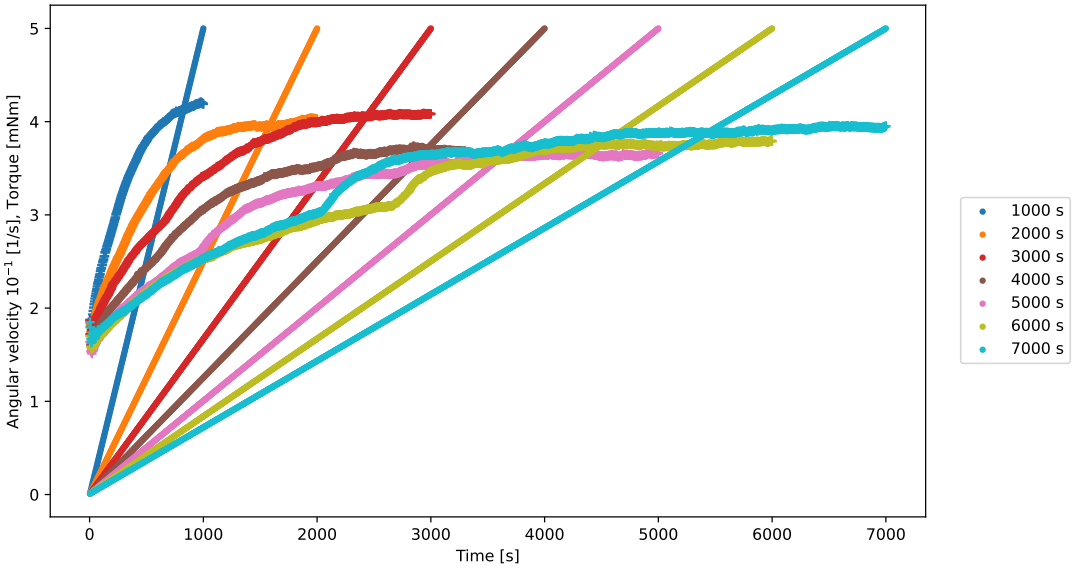

Figure 7.6: Flow curves that show the input angular velocity (straight lines) and the output torque values (curved lines) as a function of time for Exilva with a concentration of 1.86%. Every test was run from an angular velocity of 0.1 s^{-1} to 50 s^{-1}, over the specified time period. Multiple ramp-up times were tried to find the slope which gave the most reproducible results. Some noise and unexpected behavior are seen for the green and light blue curves which have sudden jumps in the torque curves at angular velocity values of 3 10^{-1} s^{-1}.

was selected to achieve reliable and reproducible results while minimizing any unwanted noise in the torque measurements.

Figure 7.8 presents the changes among angular velocity, torque, and time for Exilva with a concentration of 3.60%. The observed data exhibit pronounced fluctuations and intricate dynamics during the ramp-up phase. Notably, a ramp-up time of 28800 s demonstrated comparatively less erratic behavior. However, drawing definitive conclusions regarding the optimal ramp-up time from this graph remains inconclusive due to the complex nature of the observed variations.

7.3.3 ramp-up time dependency - Angular velocity

Additional flow curves were generated to investigate the non-Newtonian behavior of Exilva at three different concentrations: 1.86%, 2.44%, and 3.60%, with different ramp-up times. The torque values were plotted against the corresponding angular velocities to visualize the relationship between these variables.

Figure 7.9 illustrates the flow curves for Exilva with a concentration of 1.86%. The plotted data clearly exhibit a non-linear, power-law relationship between torque and angular velocity. This power-law curve shape is indicative of the non-Newtonian behavior observed in the system.

Similarly, figure 7.10 shows the flow curves for Exilva at a concentration of 2.44%. The torque values exhibit a similar power-law trend, reaffirming the

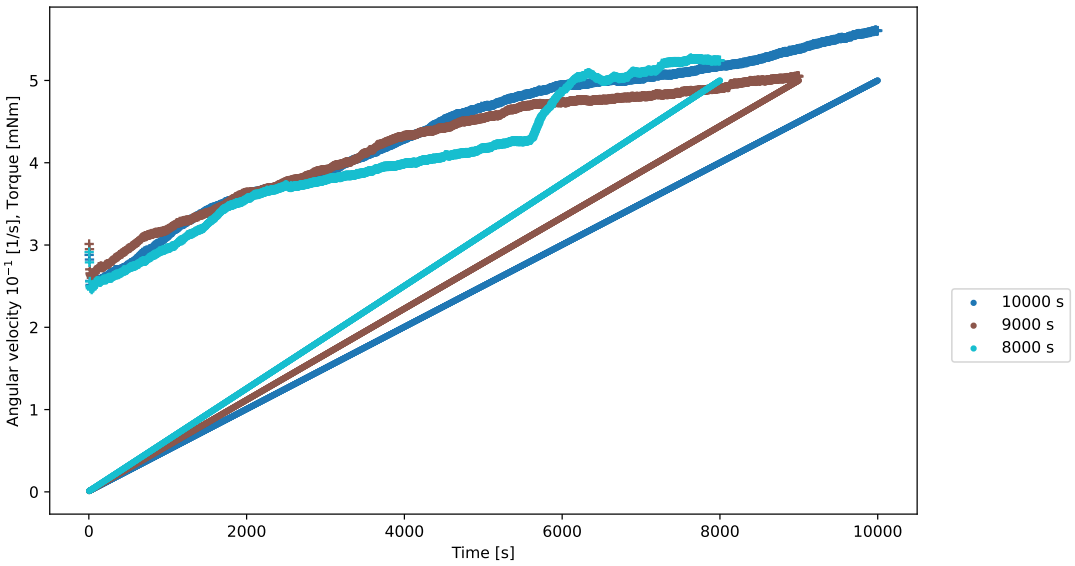

Figure 7.7: Flow curves that show the input angular velocity (straight lines) and the output torque values (curved lines) as a function of time for Exilva with a concentration of 2.44%. Every test was run from an angular velocity of 0.1 s^{-1} to 50 s^{-1}, over the specified time period. Multiple ramp-up times were tried to find the slope which gave the most reproducible results. Some noise and unexpected behavior are seen for the light blue curve which has a sudden jump in the torque curves at time 6000 s.

non-Newtonian nature of the fluid. The shape and magnitude of the curve do however vary compared to the 1.86% concentration, reflecting the influence of the different concentration levels on the material's rheological properties. The curve reinforced the decision of 9000 s as the proper ramp-up time.

In figure 7.11, the flow curves for Exilva at a concentration of 3.60% are presented. Once again, the torque-angular velocity relationship does seem to follow a power-law curve, emphasizing the non-Newtonian characteristics of the fluid at this concentration. Around an angular velocity of 20 s^{-1} the curve with a ramp-up time of 57600 s does show a sharp drop in the torque measurements and then continues on a similar power-law shape. The 10 000 and 28000 s curves have a similar drop in torque, but they happen at an angular velocity of around 40 and 45 s^{-1}. A ramp-up time of 28800 s was decided as suitable for the following experiments.

The consistent power-law curve shapes observed across the different concentrations of Exilva provide strong evidence of its non-Newtonian behavior. The deviations from linearity and the presence of power-law behavior suggest that the fluid's viscosity is dependent on the applied shear rate, rather than being constant like in Newtonian fluids.

For all ramp-up times, and all three concentrations, it is clear that an initial structure is broken down, as the torque values show a steep decrease before it shifts upwards into the shear-thinning power-law shape.

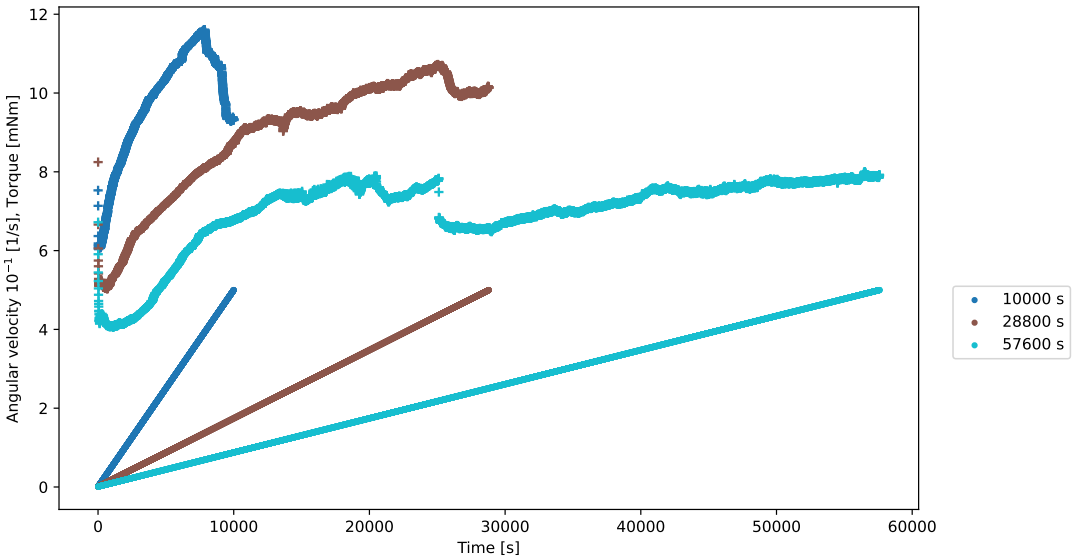

Figure 7.8: Flow curves that show the input angular velocity (straight lines) and the output torque values (curved lines) as a function of time for Exilva with a concentration of 3.60%. Every test was run from an angular velocity of 0.1 s^{-1} to 50 s^{-1}, over the specified time period. Multiple ramp-up times were tried to find the slope which gave the most reproducible results.

From the curves in section 7.3.2 and section 7.3.3, appropriate ramp-up times were chosen for each concentration. For the 1.86% concentration, a ramp-up time of 5000 seconds was deemed sufficient. For the 2.44% concentration, a ramp-up time of 9000 seconds was found to be fitting. The 3.60% concentration shows a highly complex behavior, but the ramp-up time was nevertheless set to 28800 seconds.

7.3.4 Shear rate dependency

Angular velocity and torque values were converted to shear rate and shear stress, respectively, with correction factors calculated for non-Newtonian fluids, as presented in equation (4.11) and equation (4.10).

The flow curves were constructed by plotting shear stress as a function of shear rate. Three separate parallels were considered, and their individual data points were plotted. Additionally, an average curve was generated by combining the data from the three parallels. The average is represented by a dashed black line. To indicate the transition phases, black arrows were used to represent the ramp-up and ramp-down periods. These arrows signify the direction in which the shear rate was increased or decreased, respectively.

Figure 7.12, figure 7.13, figure 7.14, show the flow curves for Exilva with a concentration of 1.86%, 2.44%, and 3.60%, respectively.

The curve for Exilva with a concentration of 1.86%, figure 7.12, shows the most consistent and least varying results between parallels. The parallels cross each

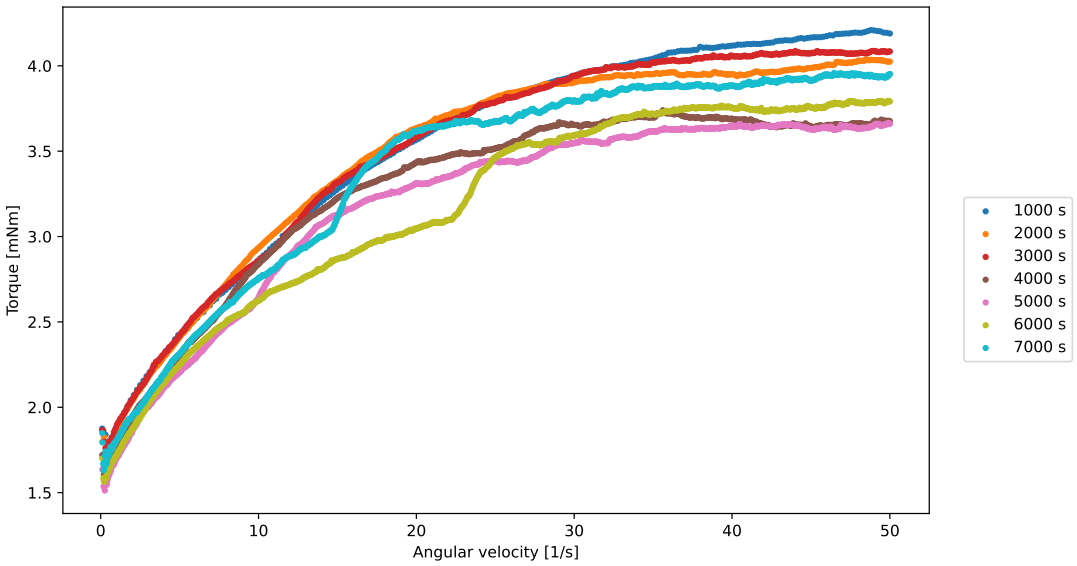

Figure 7.9: Flow curves showing torque as a function of angular velocity for Exilva with a concentration of 1.86%, with different ramp-up times. The angular velocity was increased stepwise from 0.1 s^{-1} to 50 s^{-1} during the specified time period for each curve.

other multiple times, and even though the curves aren't perfectly smooth, they do present consistency.

Compared to the 1.86% concentration, the 2.44% concentration, figure 7.13, does show a slightly more inconsistent result with larger deviations between parallels. However, the trend and shape of the curves match each other, and it seems reasonable to compute an averaged graph to counteract smaller variations.

Figure 7.14 shows the shear stress vs shear rate for Exilva with a concentration of 3.60%. It is clear that there are large deviations between the parallels when surpassing a shear rate of 25 s^{-1}. Multiple possible reasons for the deviations will be discussed. For shear rates between 0.1 and 25 s^{-1}, the parallels follow each other closely, and the decision was made to only use this shear rate range when creating models and estimating Herschel-Bulkley parameters. This was done to improve the robustness of the models, by basing it on multiple parallels.

Figure 7.15 shows the average flow curve for each concentration of Exilva. The results indicate that increasing the concentration of Exilva leads to higher shear stress at similar shear rates, suggesting a positive correlation between concentration and shear stress. Exilva also exhibits shear thinning behavior, as the rate of increase in shear stress levels off at higher shear rates.

Shear thinning behavior is further seen in the viscosity plot in figure 7.16. The viscosity decreases with increasing shear rates for all concentrations, and it is clearly demonstrated that higher concentrations lead to higher viscosities. Additionally, the hysteresis loops are demonstrated by colored arrows, corresponding to each concentration.

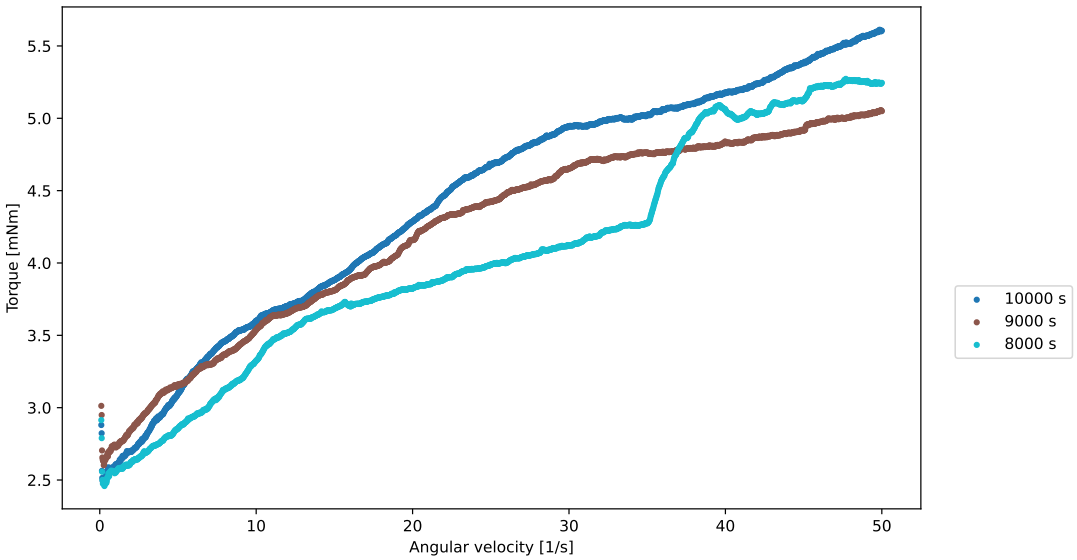

Figure 7.10: Flow curves showing torque as a function of angular velocity for Exilva with a concentration of 2.44%, with different ramp-up times. The angular velocity was increased stepwise from 0.1 s^{-1} to 50 s^{-1} during the specified time period for each curve.

7.4 Model fitting and yield point estimation

Experimental rheometer data was subjected to model fitting using a Python program. The fitting methodology and the resulting parameter estimates are presented in Table 7.6. The Herschel-Bulkley model was employed to determine the flow parameters, including the flow consistency index, K, the flow index, n, and the yield stress, τ_0. Models were computed for the ramp-up and ramp-down data separately. However, for the 3.60% concentration, only ramp-up data was consistent enough to give a reliable model, and only shear rates varying from 0.1 s^{-1} to 25 s^{-1} were used for this concentration.

The parameters K, n, and τ_0 should be regarded as interdependent data sets, as variations in one parameter can be compensated by adjustments in the other parameters. Consequently, it is not possible to compute standard deviations for individual parameters due to their interconnected nature.

The applied models predict a zero yield stress for the Exilva sample with a concentration of 1.86%. Similarly, the ramp-down phase for the Exilva sample with a concentration of 2.44% also exhibits zero yield stress. In contrast, the model predicts the presence of yield stress for the Exilva sample with a concentration of 3.60%.

Figure 7.17 presents the experimental data and the corresponding estimated model for Exilva at a concentration of 1.86%. Notably, the computed model exhibits a higher degree of smoothness, displaying minimal noise across the range of shear rates. However, both the ramp-up and ramp-down models demonstrate a tendency to underestimate the experimental data at extremely low shear rates

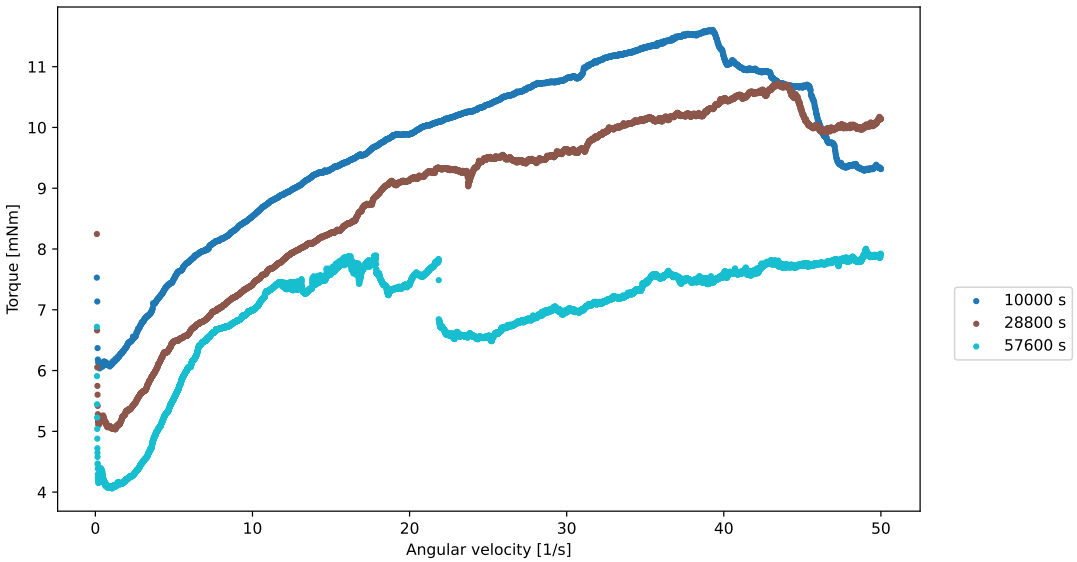

Figure 7.11: Flow curves showing torque as a function of angular velocity for Exilva with a concentration of 3.60%, with different ramp-up times. The angular velocity was increased stepwise from 0.1 s^{-1} to 50 s^{-1} during the specified time period for each curve.

when approaching the limit of zero shear rate. Conversely, for lower shear rates above 2 s^{-1}, the models tend to overestimate the shear stress until approximately 16 s^{-1}, after which they transition to slight underestimation until approximately 40 s^{-1} for the ramp-down data and approximately 50 s^{-1} for the ramp-up data. Beyond these points, the models once again surpass the experimental data, leading to an overestimation of shear stress until reaching the maximum shear rate.

Figure 7.18 illustrates the experimental data and the corresponding estimated model for Exilva with a concentration of 2.44%. Similar to the previous concentration, the computed model exhibits a smoother trend with reduced noise throughout the range of shear rates. The ramp-up model exhibits an underestimation of the experimental data at low shear rates. From approximately 3 s^{-1} to 14 s^{-1}, the model follows the experimental data, but beyond this range, it demonstrates an overshooting tendency. The overshooting persists until around 30 s^{-1}, where the model once again aligns with the experimental data. However, at shear rates exceeding 55 s^{-1}, the model surpasses the experimental data, remaining consistently above it, until reaching the maximum shear rate.

Conversely, the ramp-down model approaches the same yield stress as observed in the experimental data. It initially overestimates the shear stress until approximately 13 s^{-1}. Subsequently, it transitions to an undershoot, persisting until approximately 48 s^{-1}. Beyond this point, the model once again surpasses the experimental data, remaining consistently above it.

Figure 7.19 illustrates the experimental data and the corresponding estimated model for Exilva with a concentration of 3.60%. The model only includes ramp-

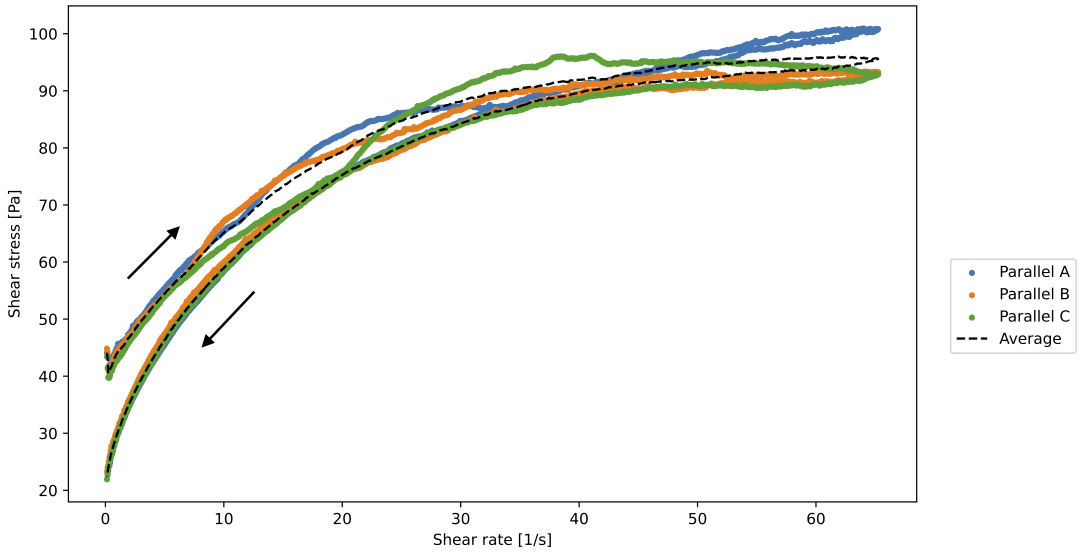

Figure 7.12: Flow curve showing shear stress as a function of shear rate for three parallels of Exilva with a concentration of 1.86%. In addition, an average curve was generated from the three parallels, which is plotted as a dashed black line. The shear rate was increased step-wise on a linear scale from $0.1s^{-1}$ to $65s^{-1}$. The black arrows show the direction of the ramp-up and the ramp-down.

up data from angular velocities between 0.1 s^{-1} and 25 s^{-1}, corresponding to a shear rate of approximately 35 s^{-1}. This means at higher shear rates, the model is extrapolated and not based on experimental measurements, which weakens the model above shear rates of 25 s^{-1}. The model follows the experimental data closely from a shear rate of 5 s^{-1} to 27 s^{-1}. At elevated shear rates, the model exhibits a tendency to overestimate the shear stress. At lower shear rates, the model fails to capture the initial structural breakdown, resulting in the incorrect prediction of the yield stress. However, it is important to note that the Herschel-Bulkley model, as outlined in section 4.8.1, is not inherently designed to capture the initial decrease in shear stress followed by a subsequent increase.

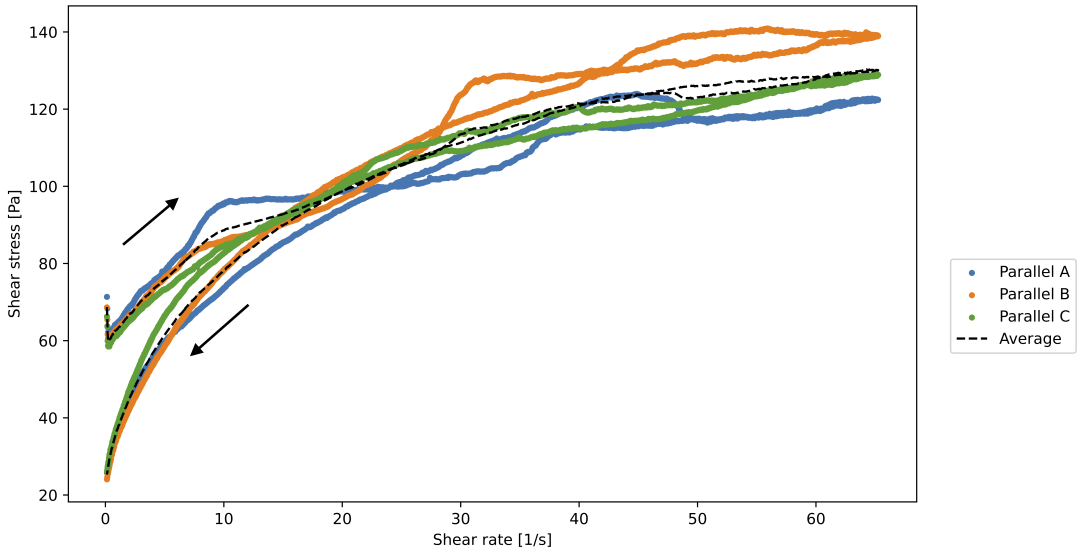

Figure 7.13: Flow curve showing shear stress as a function of shear rate for three parallels of Exilva with a concentration of 2.44%. In addition, an average curve was generated from the three parallels, which is plotted as a dashed black line. The shear rate was increased step-wise on a linear scale from $0.1s^{-1}$ to $65s^{-1}$. The black arrows show the direction of the ramp-up and the ramp-down.

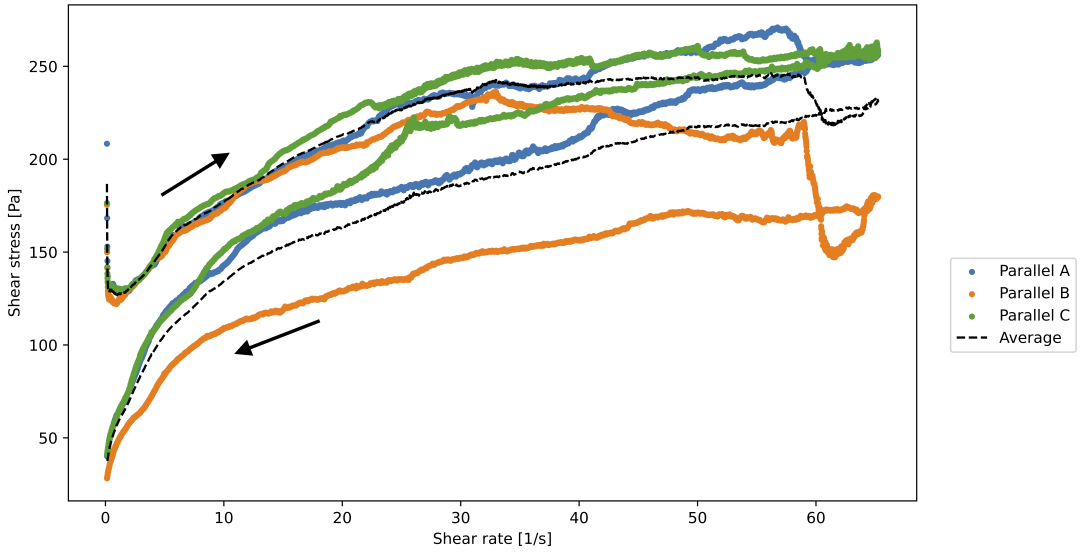

Figure 7.14: Flow curve showing shear stress as a function of shear rate for three parallels of Exilva with a concentration of 3.60%. In addition, an average curve was generated from the three parallels, which is plotted as a dashed black line. The shear rate was increased step-wise on a linear scale from $0.1s^{-1}$ to $65s^{-1}$. The black arrows show the direction of the ramp-up and the ramp-down.

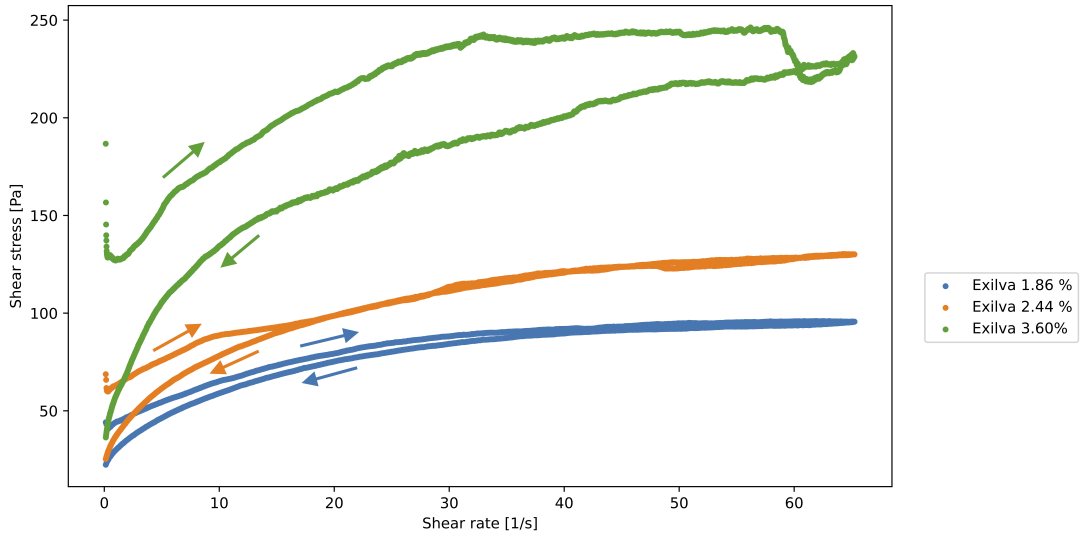

Figure 7.15: Flow curve showing shear stress as a function of shear rate for three Exilva samples of different concentrations. The shear rate was increased step-wise on a linear scale from $0.1s^{-1}$ to $65s^{-1}$. Colored arrows show the ramp-up and ramp-down for each concentration, corresponding to the colors presented in the legend.

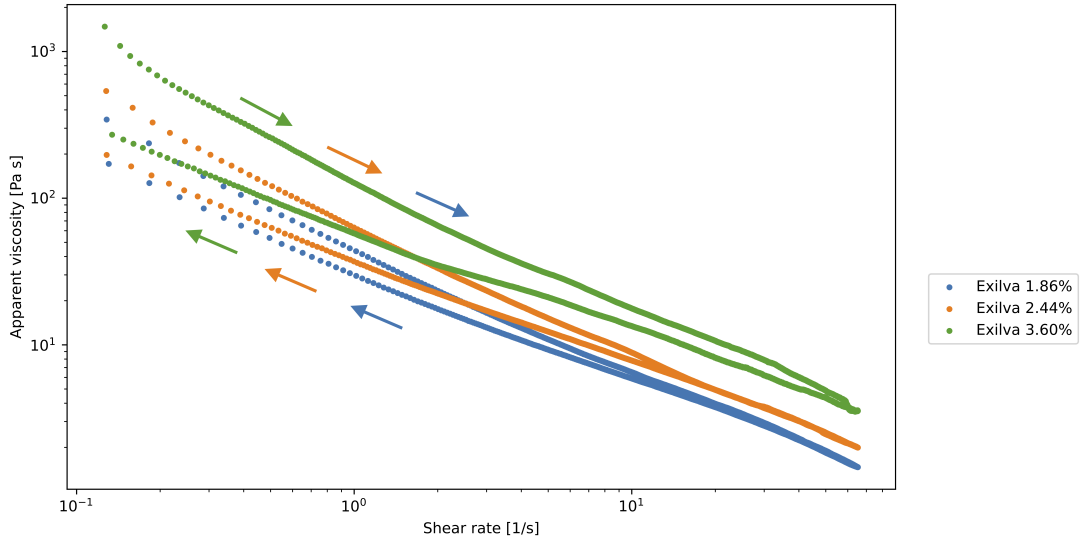

Figure 7.16: Viscosity plot showing viscosity as a function of shear rate on a log-log plot for three Exilva samples of different concentrations. The shear rate was increased step-wise on a logarithmic scale from $0.1s^{-1}$ to $65s^{-1}$. Colored arrows show the ramp-up and ramp-down for each concentration, corresponding to the colors presented in the legend. Note the logarithmic scale on both the x- and y-axis.

Table 7.6: Model fitting with parameters generated by a Python optimization program. The program tests different methods based on the root mean square error. The best-fitting model with the lowest chi-square value is used to determine the parameters. The table summarizes which method was used, which model was used to fit the data and the parameter values found by that specific model. τ_0 is the yield stress $[Pa]$, K is the flow consistency index $[Pa \cdot s^n]$, and n is the flow index $[-]$. Up and down refers to the ramp-up and ramp-up data that the calculations are based on. As previously presented, for the 3.60%, only the ramp-up data with shear rates from 0.1-25 is used.

Material	**Method**	**Model**	$\tau_0[Pa]$	$K[Pas^n]$	n
Exilva 1.86% up	Dual annealing	Herschel-Bulkley	0.0	41.58	0.21
Exilva 1.86% down	Dual annealing	Herschel-Bulkley	0.0	32.85	0.27
Exilva 2.44% up	Dual annealing	Herschel-Bulkley	43.09	18.55	0.38
Exilva 2.44% down	Dual annealing	Herschel-Bulkley	0.0	41.51	0.28
Exilva 3.60% up	Dual annealing	Herschel-Bulkley	108.13	18.40	0.58

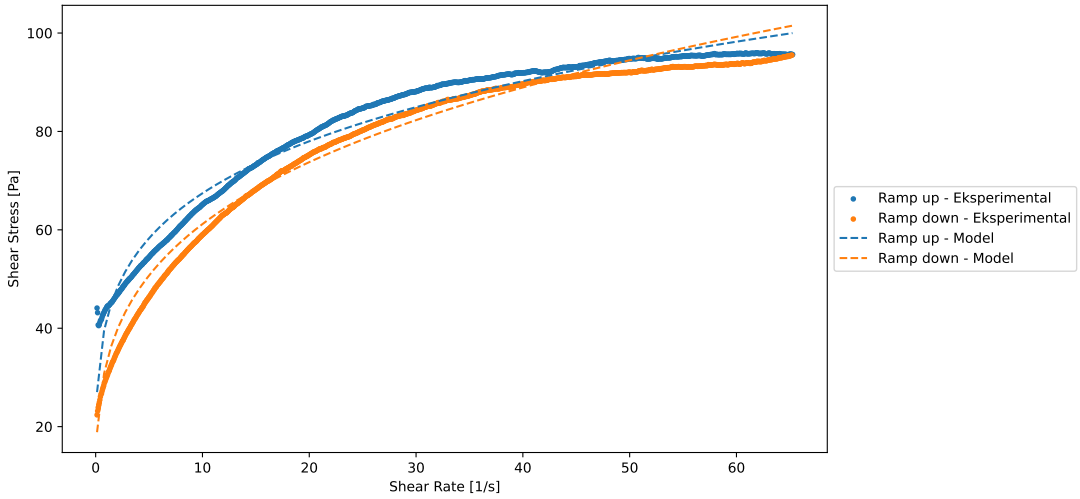

Figure 7.17: Flow curve of Exilva with a concentration of 1.86% with the addition of model fitting curves generated by parameter estimation with the Herschel-Bulkley model. The methods and parameters for each curve are summarized in table 7.6.

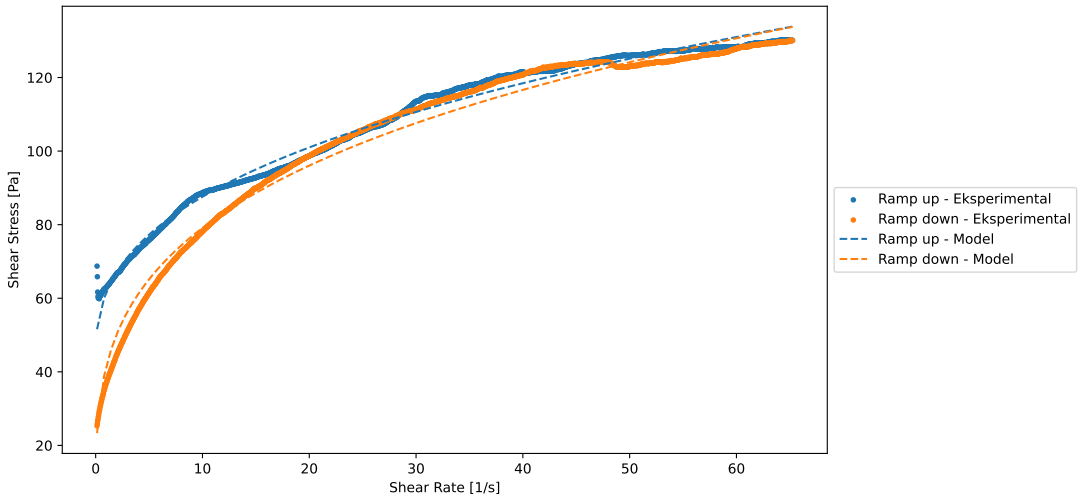

Figure 7.18: Flow curve of Exilva with a concentration of 2.44% with the addition of model fitting curves generated by parameter estimation with the Herschel-Bulkley model. The methods and parameters for each curve are summarized in table 7.6.

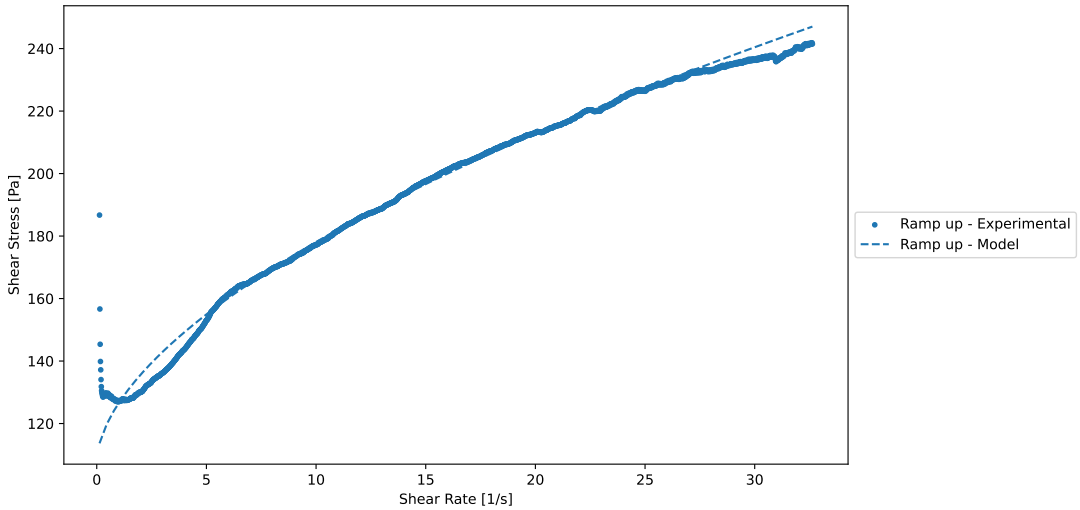

Figure 7.19: Flow curve of Exilva with a concentration of 3.60% with the addition of model fitting curves generated by parameter estimation with the Herschel-Bulkley model. Only ramp-up data from angular velocities varying from 0.1 s^{-1} to 25 s^{-1} were used for this concentration. The methods and parameters for each curve are summarized in table 7.6.

8 Results - Pipe rig

The subsequent section presents precise data solely from the experiment conducted on Exilva with a concentration of 3.60%, utilizing a 2.88 cm diameter pipe with a length of 4.79 meters. This particular experiment was selected due to its exemplification of the most extreme scenario, resulting in the highest and most visible pressure difference. Model fitting and parameter estimation include all experiments with varying concentrations, pipe lengths, and pipe diameters.

8.1 Flow rate and flow velocity

During each experimental configuration, the mass and pressure differences were documented throughout the flow duration. The mass values were subjected to analysis to ascertain the flow rate. Figure 8.1 illustrates the recorded mass for each pump speed against time. The slope of the plotted curves corresponds to the mass flow rate expressed in kilograms per second.

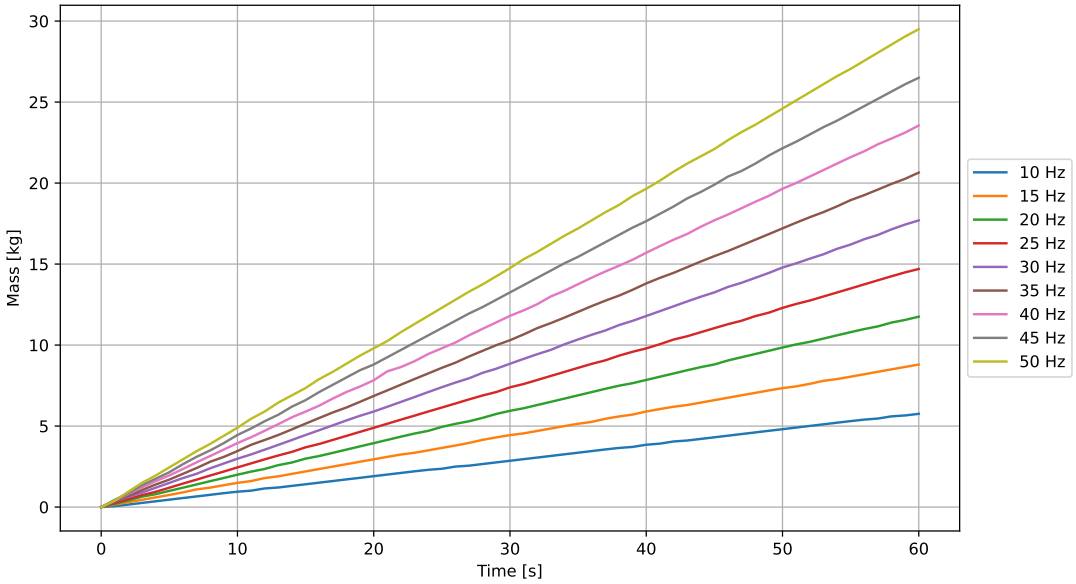

Figure 8.1: Recorded mass over time for each pump speed. The plot shows data from the experiments involving a 3.60% Exilva material, in the 2.88 cm diameter pipe with a length of 4.79 meters.

The flow rates obtained from the experimental data illustrated in figure 8.1 were subjected to further analysis to convert them into flow velocities, which were then plotted against the corresponding pump speeds. Additionally, the measurements recorded during the experiment were utilized to calculate the standard deviation within each specific pump speed setting.

Figure 8.2 visually represents the relationship between the flow velocity and the pump speed, showcasing the inherent variability in the measurements. To provide a comprehensive evaluation of the data, error bars corresponding to the standard deviation were incorporated into the plot.

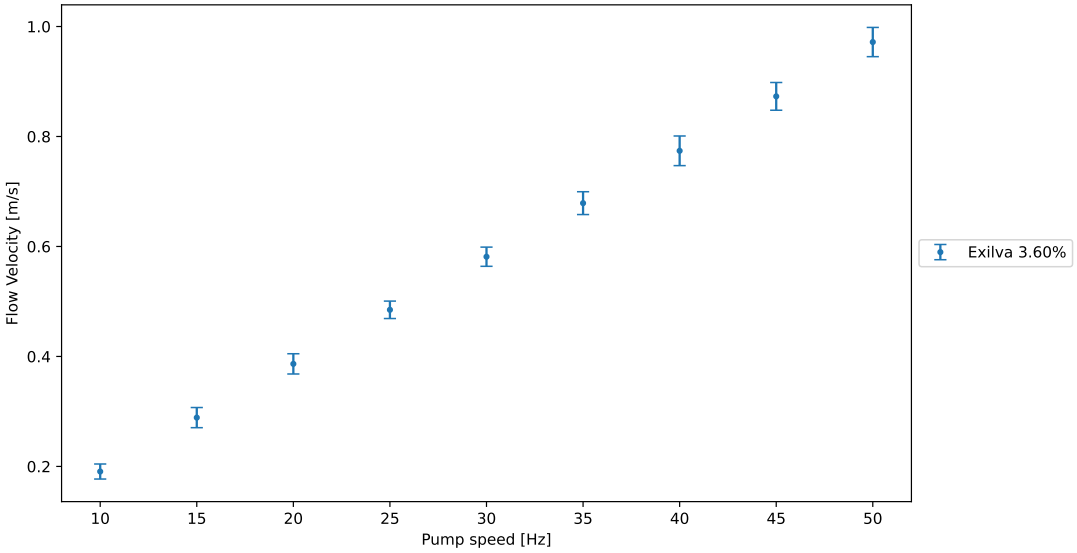

Figure 8.2: Illustration of the relationship between the calculated flow velocity and the pump speed (expressed in Hz) for the specific experiment conducted on Exilva with a concentration of 3.60%, utilizing a pipe with a diameter of 2.88 cm and a length of 4.79 meters. The data points represent the flow velocities obtained at various pump speeds during the experiment, including error bars based on the standard deviation.

8.2 Pressure drop

Pressure measurements are susceptible to noise and fluctuations during the course of the experiment. Figure 8.3 visually depicts the evolution of the pressure difference observed between the two sensors for various pump speeds. It is evident that increasing the pump speed leads to greater pressure drops. Moreover, except for minor fluctuations, it is apparent that the pressure drop remains relatively constant at consistent pump speeds.

The average pressure drop was computed for each pump speed, accompanied by the calculation of standard deviations to account for variations in the measurements. Figure 8.4 showcases the mean pressure drop along with the corresponding variations plotted as error bars. This representation allows for comprehensive visualization of the average pressure drop and the associated uncertainties across different pump speeds.

8.3 Model fitting and yield point estimation

The model fitting process was carried out using a proprietary Python script, employing a methodology inspired by the work of Slatter and Co[39]. The model assumes a pipe plug flow and employs optimization techniques to estimate the Herschel-Bulkley parameters. Due to confidentiality reasons, the specific details of the model's implementation are not disclosed, and it is considered a black box model. The model is designed to accommodate experiments conducted with

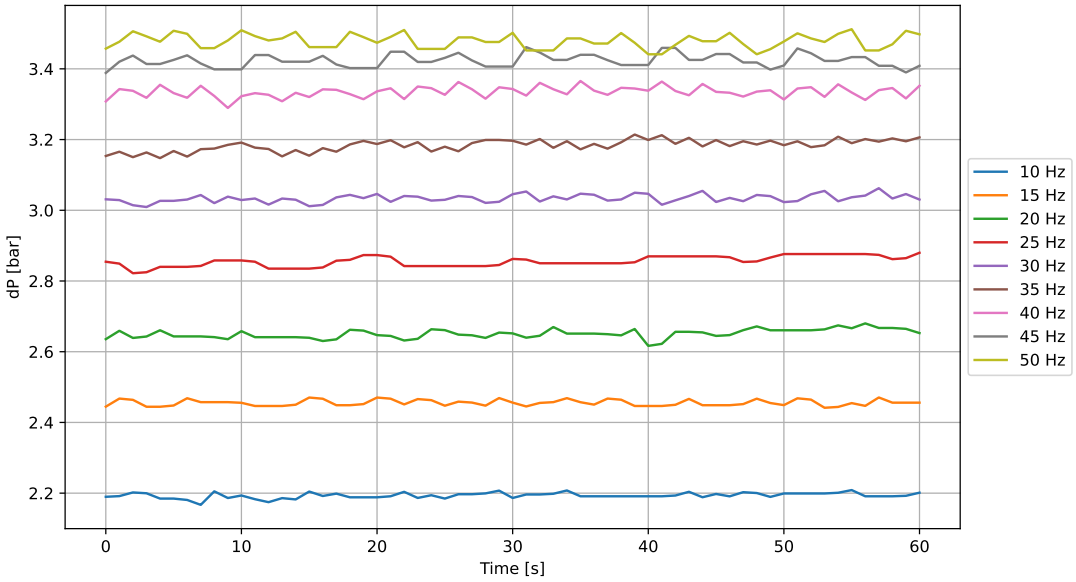

Figure 8.3: Recorded pressure drop over time for each pump speed. The plot shows data from the experiments involving a 3.60% Exilva material, in the 2.88 cm diameter pipe with a length of 4.79 meters.

various pipe lengths, pipe diameters, and flow rates, allowing it to determine the most suitable model parameters through the fitting process.

Regrettably, the short pipe experiments exhibited significant fluctuations in the obtained data. The pipe length is present in calculations as a linear step, indicating that longer pipes offer enhanced stability and reproducibility. Nevertheless, the determination of the Herschel-Bulkley parameters encompassed all experimental data encompassing various pipe length configurations. This approach aimed to construct models based on a comprehensive dataset, thereby enhancing the reliability and consistency of the outcomes.

Due to the utilization of only a single pipe diameter in the experimental setup for Exilva with a concentration of 1.86%, it is hard to compute Herschel-Bulkley parameters that possess broader applicability. The limited scope of employing only one diameter and two lengths restricts the generalizability of the obtained results, as they pertain solely to the specific experimental configuration utilized in this study. The availability of multiple pipe diameters and lengths allows for a more comprehensive estimation of the Herschel-Bulkley parameters, enhancing the reliability and applicability of the computed results. The results from the model fitting are found in table 8.1.

8.4 Calculated pressure drop from estimated Herschel-Bulkley parameters

The Herschel-Bulkley parameters were estimated and utilized for the reverse calculation of the anticipated pressure drop corresponding to each pump speed. This

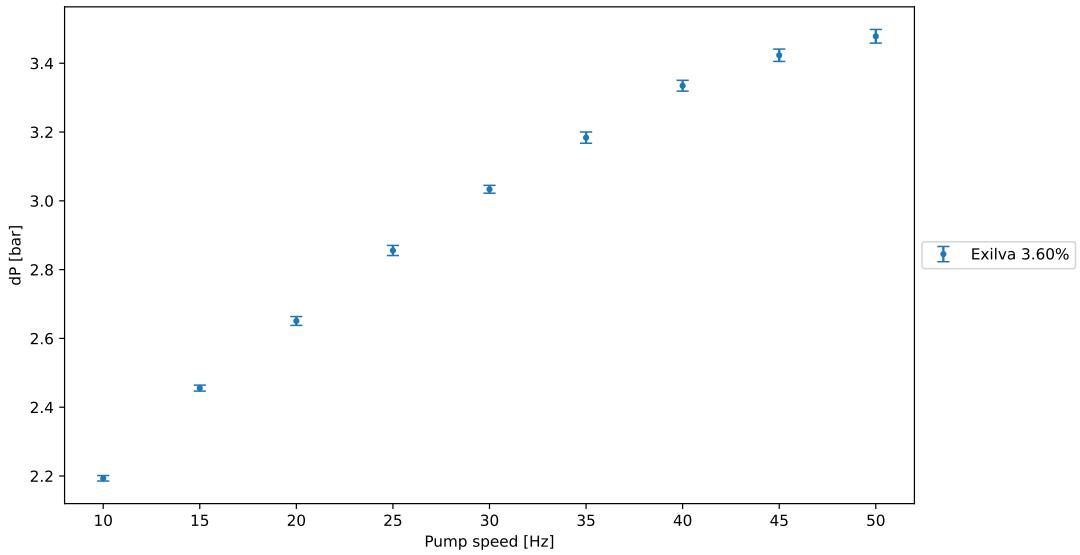

Figure 8.4: Illustration of the relationship between the measured pressure drop and the pump speed (expressed in Hz) for the specific experiment conducted on Exilva with a concentration of 3.60%, utilizing a pipe with a diameter of 2.88 cm and a length of 4.79 meters. The data points represent the pressure drop obtained at various pump speeds during the experiment, including error bars based on the standard deviation.

section exclusively presents the computed pressure drops based on the identical experimental arrangement depicted in figure 8.2 and figure 8.4, namely Exilva with a concentration of 3.60%, utilizing a 2.88 cm diameter pipe with a length of 4.79 meters.

Figure 8.5 displays the relationship between the calculated pressure drop values and the corresponding experimentally measured pressure drops. The blue data points on the plot represent the calculated pressure drop values, while the orange dashed line represents a linear relationship with a slope of 1.

By examining the position of the data points relative to the orange dashed line,

Table 8.1: Model fitting with parameters generated by a Python optimization program. The program tests different methods based on the root mean square error. The best-fitting model with the lowest chi-square value is used to determine the parameters. The table summarizes which method was used, which model was used to fit the data and the parameter values found by that specific model. τ_0 is the yield stress $[Pa]$, K is the flow consistency index $[Pa \cdot s^n]$, and n is the flow index $[-]$. For the 1.86% concentration, only the small diameter pipe was used to estimate the parameters.

Material	**Method**	**Model**	$\tau_0[Pa]$	$K[Pas^n]$	n
Exilva 1.86 %	Dual annealing	Herschel-Bulkley	41.04	10.62	0.40
Exilva 2.44 %	Dual annealing	Herschel-Bulkley	0.1	47.38	0.26
Exilva 3.60 %	Dual annealing	Herschel-Bulkley	132.60	37.08	0.41

we can assess the level of agreement between the calculated and experimentally measured values. Ideally, if the calculated pressure drop values perfectly matched the experimentally measured values, all the data points would lie precisely on the orange dashed line. Deviations from this line indicate discrepancies between the calculated and measured results.

This plot serves as a valuable tool to evaluate the accuracy and reliability of the calculations. It provides crucial insights into the performance of the model and can guide further analysis and refinement of the model to improve its predictive capabilities.

To assess the predictive performance of the model, two statistical metrics, namely the R-squared value, and root mean square error (RMSE), were computed for the dataset. The obtained R-squared value is 0.98, indicating a high degree of correlation between the predicted pressure drop and the experimental data points. The RMSE value, calculated as 0.051, represents the average magnitude of the residuals, providing a measure of the model's accuracy.

These results suggest that the model used to derive the calculated pressure drop demonstrates a strong correspondence with the experimental data. The high R-squared value indicates that the model captures a significant portion of the variance present in the dataset. Additionally, the low RMSE value signifies that the predicted pressure drop values closely align with the observed experimental measurements.

8.5 Comparison of parallels to ensure consistency

To ensure the reliability and consistency of the experimental results, the testing setup incorporated the use of parallels. A parallel experiment was conducted on Exilva with a concentration of 3.60%, utilizing a 5.5 cm diameter pipe with a length of 4.79 meters. This methodology allowed for a thorough examination of the experimental conditions, investigating the potential impact of random errors and providing a means to validate the consistency of the obtained results. Parallel A was conducted in the early stages of the testing, while parallel B was conducted towards the end of experimental testing.

8.5.1 Flow velocity

Figure 8.6 shows the flow velocity against the pump speed for two parallels with the previously described setup. It is clearly seen that the flow velocity showed great consistency between the two parallels throughout all flow speeds.

8.5.2 Pressure drop

Figure 8.7 displays the relationship between pressure drop and pump speed for two parallel setups within the aforementioned experimental configuration. The pressure drop exhibits consistent behavior across both parallels until a pump

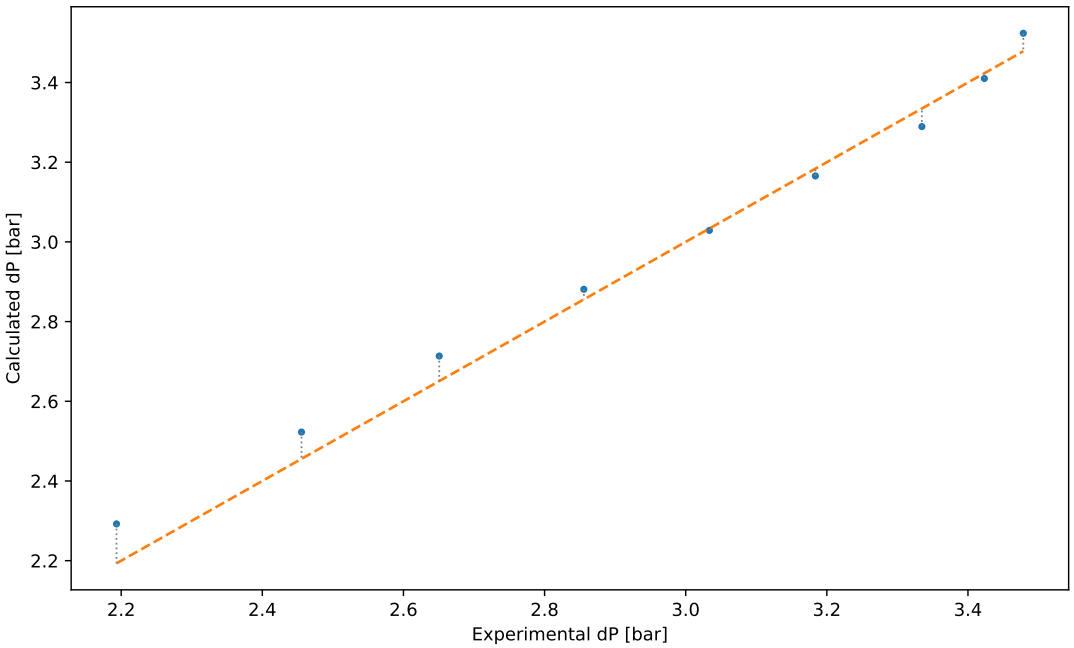

Figure 8.5: The plot illustrates the comparison between the calculated and experimentally measured pressure drops for Exilva at a concentration of 3.60%, with a pipe length of 4.79 m and a pipe diameter of 2.88 cm. The data points, shown as blue dots, depict the calculated pressure drop corresponding to the measured pressure drop. The orange dashed line represents a linear relationship with a slope of 1. This implies that if the calculated pressure drop values perfectly match the experimentally measured values, all the data points would align precisely along the orange dashed line.

speed of 35 Hz is reached. At this point, the earlier parallel (A) demonstrates a higher pressure drop compared to the later parallel (B). Notably, parallel A exhibits an anomalous behavior at higher pump speeds, where the pressure drop at 45 Hz is higher than that at 50 Hz.

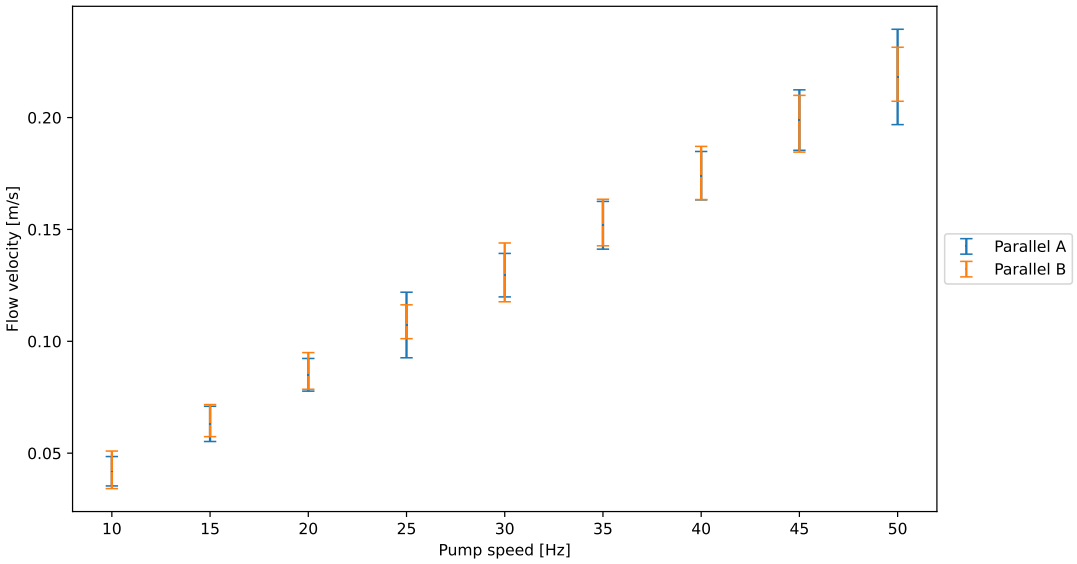

Figure 8.6: Flow velocity as a function of pump speed in Hz for two parallels with identical setups. The setup consists of Exilva with a concentration of 3.60%, pipe length of 4.79 m, and pipe diameter of 5.5 cm.

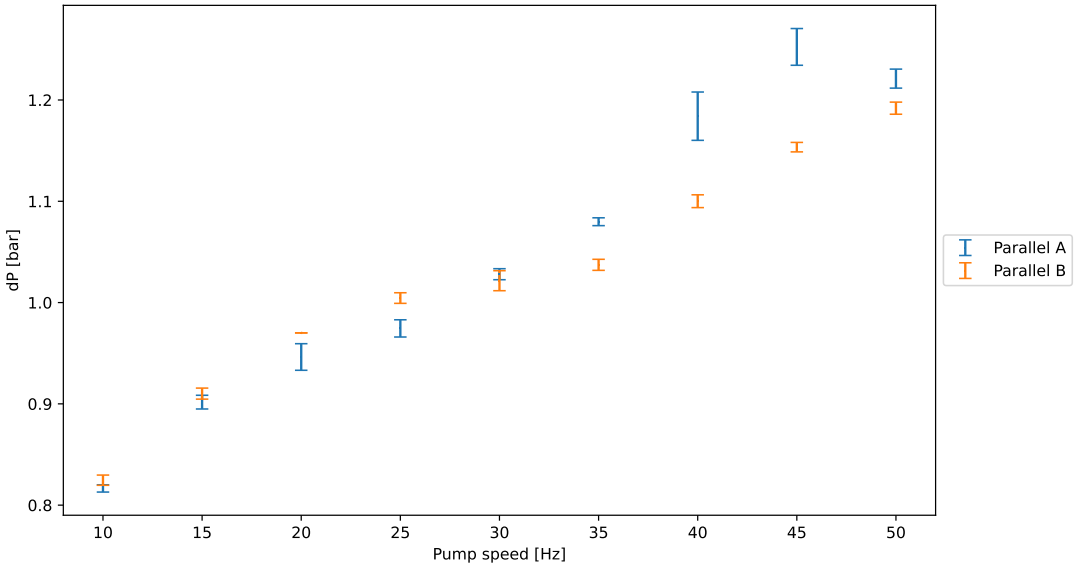

Figure 8.7: Pressure drop as a function of pump speed in Hz for two parallels with identical setups. The setup consists of Exilva with a concentration of 3.60%, pipe length of 4.79 m, and pipe diameter of 5.5 cm.

9 Results - Rheometer vs pipe rig

The computed Herschel-Bulkley parameters obtained from the rheometer and pipe rig experiments have been presented in previous sections. This section focuses on comparing the characterization of fluid flow parameters using the two methods. Graphs incorporate experimental data from the rheometer as well as models computed from both the rheometer data and the pipe rig data. The aim is to analyze and contrast the results obtained from these two approaches in characterizing fluid flow behavior. By examining these comparisons, insights can be gained regarding the similarities and differences between the two methods of characterizing fluid flow parameters.

Figure 9.1, figure 9.2, and figure 9.3 display the experimental shear stress and shear rate data obtained from rheometer experiments conducted on Exilva with concentrations of 1.86%, 2.44%, and 3.60%. The blue and orange dots correspond to the ramp-up and ramp-down tests, respectively. Complementary to the experimental data, the dashed blue and orange lines depict the models derived from the rheometer data. Lastly, the green dashed line corresponds to the model derived from experiments performed on the pipe rig.

The figures allow for a visual comparison of the different models and their agreement with the experimental data, providing valuable insights into the performance and accuracy of each approach in capturing the shear stress and shear rate relationship for the fluid.

Figure 9.1 presents a comparison of various models for Exilva with a concentration of 1.86%. The figure showcases the deviations observed among the models and their agreement with the experimental data. The pipe rig model exhibits a favorable correspondence with both the experimental data and the models based on rheometer experiments. Notably, the pipe rig model demonstrates a slight overestimation of shear stress at lower shear rates, but closely follows the trend beyond 20 s^{-1}.

Figure 9.2 provides a comparative analysis of different models for Exilva with a concentration of 2.44%. The figure highlights the observed variations among the models and their agreement with the experimental data.

The pipe rig model demonstrates a good correspondence with both the experimental data and the models based on rheometer experiments. Notably, the pipe rig model exhibits a minor overestimation of shear stress at shear rates exceeding 15 s^{-1}. However, at lower shear rates, it aligns between the ramp-up and ramp-down models derived from the rheometer experimental data.

Figure 9.3 depicts multiple models employed to analyze Exilva at a concentration of 3.60%. The figure emphasizes the variations observed among the models and their respective levels of agreement with the experimental data.

The pipe rig model displays an overshoot when compared to the experimental data. While the model appears to capture the yield stress, it surpasses the an-

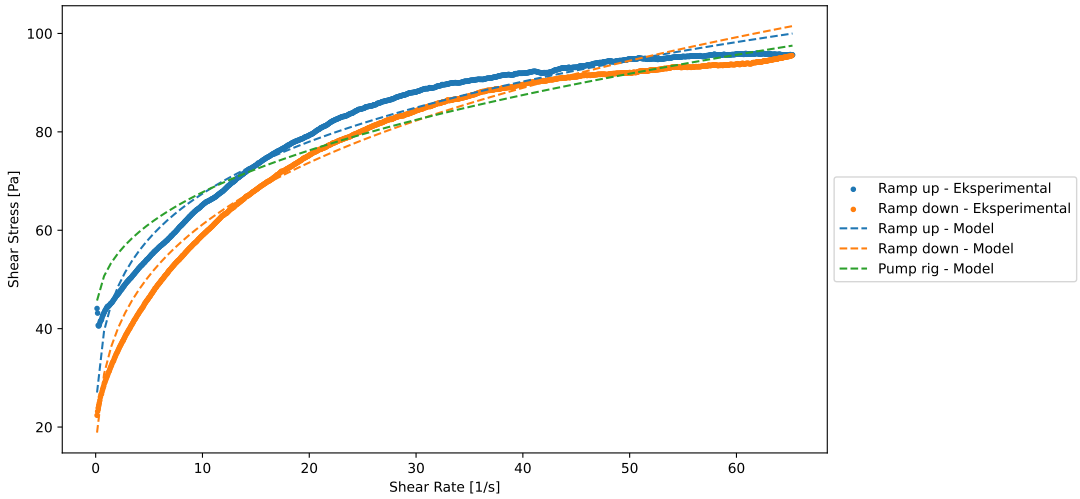

Figure 9.1: Experimental shear stress and shear rate data obtained from rheometer experiments conducted on Exilva with a concentration of 1.86%. The data points are represented by blue dots for the ramp-up phase and orange dots for the ramp-down phase. The dashed blue and orange lines correspond to the models computed using the rheometer data, providing a representation of the fluid's behavior based on the original measurements. The green dashed line represents the model computed from experiments conducted on the pipe rig.

ticipated shear stress at shear rates above zero. This observation may indicate that the rheometer underestimates shear stresses for materials with high concentrations, such as Exilva at a concentration of 3.60%. The disparity between the rheometer and pipe rig will be comprehensively examined in section 10.

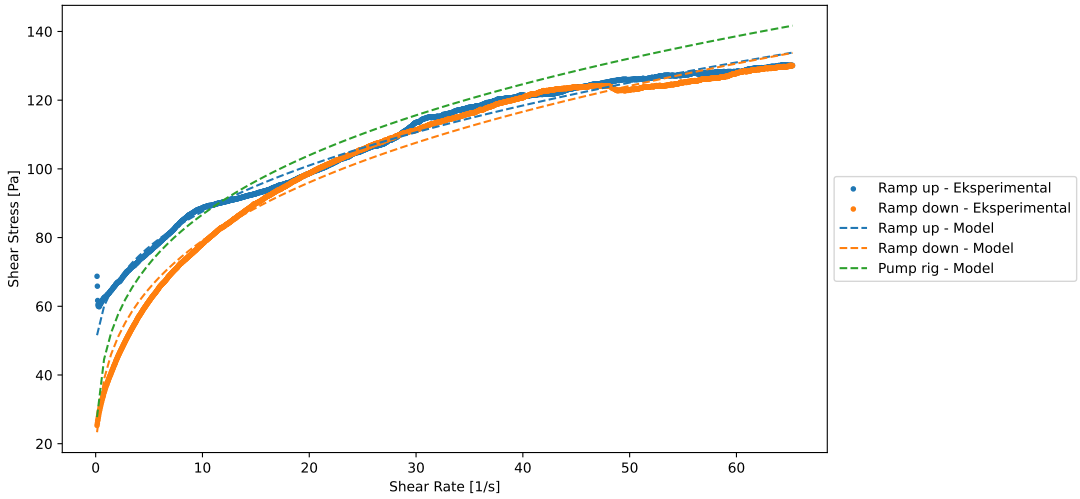

Figure 9.2: Experimental shear stress and shear rate data obtained from rheometer experiments conducted on Exilva with a concentration of 2.44%. The data points are represented by blue dots for the ramp-up phase and orange dots for the ramp-down phase. The dashed blue and orange lines correspond to the models computed using the rheometer data, providing a representation of the fluid's behavior based on the original measurements. The green dashed line represents the model computed from experiments conducted on the pipe rig.

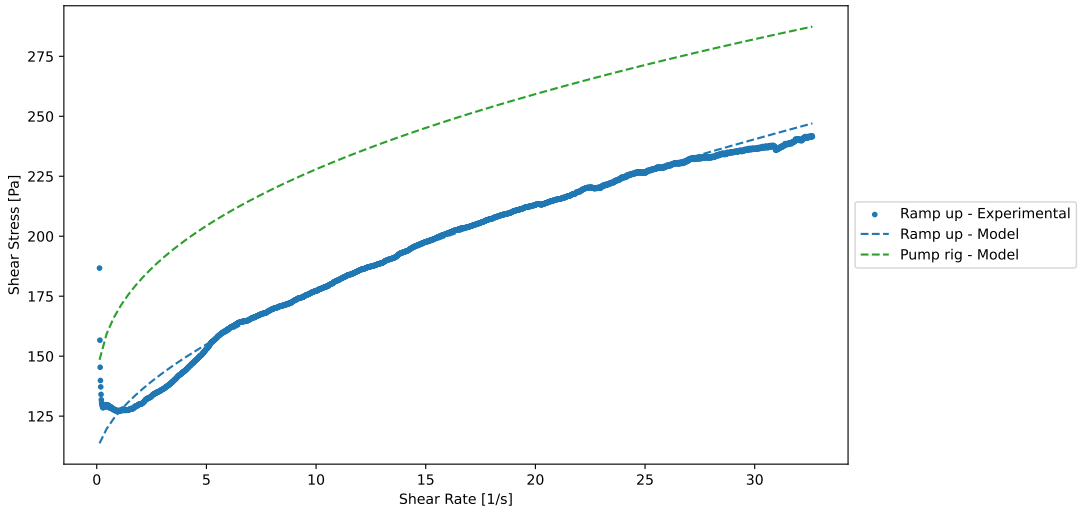

Figure 9.3: Experimental shear stress and shear rate data obtained from rheometer experiments conducted on Exilva with a concentration of 3.60%. The data points are represented by blue dots for the ramp-up, while the dashed blue line corresponds to the model computed using the rheometer data, providing a representation of the fluid's behavior based on the original measurements. The green dashed line represents the model computed from experiments conducted on the pipe rig.

10 Discussion

The discussion section of this thesis encompasses three distinct areas, each corresponding to the results obtained from different testing methods. The first area focuses on the analysis of rheometer testing, providing insights into the behavior of the material under controlled rotational conditions. The second area delves into the examination of pipe rig testing, exploring the performance of the material in a more realistic flow environment. Lastly, the third area involves a comprehensive comparison and evaluation of the results obtained from both testing methods, aiming to identify any similarities and discrepancies. By addressing these three distinct areas, this discussion section aims to provide a comprehensive analysis of the experimental findings and contribute to a deeper understanding of the material's rheological properties and its response to different testing methodologies.

10.1 Rheometer

Multiple challenges were encountered and interesting results were found during the rheometer testing. This section aims to discuss and evaluate these findings.

10.1.1 Flow behavior

The flow behavior of Exilva was investigated using three samples with concentrations of 1.86%, 2.44%, and 3.60% DS. Controlled shear rate testing was conducted to assess the rheological properties of the samples. The results demonstrated that all samples exhibited non-Newtonian shear thinning flow behavior. Specifically, as the shear rate increased, the shear stress increased while the viscosity decreased. This behavior is characteristic of non-Newtonian shear-thinning fluids. Moreover, the findings align with previous research and information provided by the producer of Exilva, Borregaard. Similar shear thinning behavior for MFC suspensions has been reported and noted that higher concentrations resulted in both higher shear stress and higher viscosity[14]. This observation is consistent with the expected behavior, as higher concentrations of Exilva lead to greater resistance to flow.

The agreement between the experimental results and the information from Borregaard's reports[13][12] supports the validity and reliability of the obtained data, further reinforcing the understanding of Exilva's rheological properties.

10.1.2 Vane effective dimensions and container size

The effective dimensions of vanes, including the effective height and radius, play a crucial role in determining flow resistance in rheometer experiments. In this study, the effective dimensions of three vane sizes, namely V80/40, V40/20, and V10/5, were investigated. The results indicated variations in the effective dimensions between different vane sizes and containers.

For the V80/40 vane, there was a close agreement in the estimated effective radius between the small and large containers, differing by only 0.04 cm. However, a more significant difference of 0.65 cm was observed in the effective height, corresponding to a relative increase of 7.1% when transitioning from the small to the large container. These variations suggest that container size can influence the determination of effective dimensions.

Similarly, for the V40/20 vane, the effective height exhibited great consistency across the two containers, with a variation of only 0.11 cm and a relative decrease of 2.7% when transitioning from the small to the large container. On the other hand, the effective radius showed a more significant deviation of 0.09 cm, corresponding to a relative increase of 10.3% in the large container. These findings highlight the importance of considering container size when determining the effective dimensions of vanes.

It should be noted that the accuracy and reliability of the results varied depending on the vane size. The V10/5 vane exhibited larger variations, leading to concerns about the reliability and accuracy of the obtained data. Consequently, further experiments with this vane were not conducted.

Furthermore, the submersion depth of the vane within the fluid also plays a role in the determination of effective dimensions. In both the V80/40 and V40/20 vanes, the linear regression analysis considered values only when the non-wetted height was above zero. This decision was made as the linear relationship between flow resistance and non-wetted height does not extend beyond this range. However, it was suggested that further experiments with the vane fully submerged in the sample (y=0) could provide more reliable results.

The influence of container size and submersion depth on the effective dimensions can be attributed to the variations in flow dynamics and fluid behavior within different containers and at different submersion depths. Fluid flow near container walls, and the interaction between the vane and the fluid, can be influenced by the container and size submersion level. These factors can lead to differences in flow resistance and affect the determination of effective dimensions. However, one study has shown that the container size does not show a large effect on the yield stress[45], which could indicate that it shouldn't interfere with determining the effective dimensions of vanes either. The experiments in the study involved multiple larger containers, suggesting that in future work, more container sizes should be tested to investigate the possible relationship with the vane effective dimensions.

10.1.3 Weissenberg effect and vane submersion

The experimental setup initially aimed for a vane depth of 0 cm within the fluid medium. However, this approach resulted in significant noise and non-reproducibility, which were mainly thought to be attributed to the observed Weissenberg effect. The impact of the Weissenberg effect was particularly pro-

nounced at higher concentrations and viscosities. The presence of this effect hindered the accurate measurement and interpretation of flow properties.

To overcome these issues and enhance the reproducibility of the experimental setup, an alternative approach was adopted. Instead of maintaining a vane depth of 0 cm, the vane was submerged to a depth of y = -0.5 cm. This adjustment was found to effectively mitigate the disadvantages associated with the Weissenberg effect, resulting in improved reproducibility of the experimental outcomes. Recognizing that submerging the vane to a depth of y = -0.5 cm resulted in some extra resistance on the vane shaft is important. However, this resistance was thought to be minimal when compared to the full resistance of the vane.

10.1.4 Evaporation during long-lasting experiments

Long-duration experiments conducted with rotational rheometers can be susceptible to the issue of evaporation, which can have significant implications for the accuracy and reliability of the obtained results. In rotational rheometry with vane geometries, the sample being tested is placed within a confined container with no top seal. Evaporation can introduce several complications in the experimental setup. Firstly, the loss of liquid components due to evaporation leads to a change in the concentration or composition of the sample. This alteration can significantly affect the rheological behavior and result in inaccurate measurements.

Following the completion of extended experiments, the presence of solidified material on the inner walls of the test containers provided evidence of the significant impact of evaporation. Solidified material can be seen on the side of the container shown in figure 10.1. An effort was put into minimizing the evaporation by placing the rheometer in a room with no extra ventilation and placing aluminum foil across the top to trap moisture.

The complex flow behavior observed for Exilva with a concentration of 3.60% may be partly due to evaporation. The background for this hypothesis is the very long experiment times of 16 hours in total (8-hour ramp-up and 8-hour ramp-down). The hypothesis includes drawing parallels from the distinguished sudden drops in shear stress during ramp-up, to more solid-like materials which may suffer from plastic deformation. Plastic deformation results in a permanently distorted shape, meaning the material won't be able to regain its original shape [46]. Generally, plastic deformation is a mechanical property for solid-like materials, which is not directly applicable to fluid-like materials. However, it does seem that at higher shear rates, the shear stress of the 3.60% concentration drops, seemingly acting like a fracture in the structure of the material. Deformation of the structure could explain why the shear stress experiences a step-decrease since it won't be sheared the same way after fracturing. This hypothesis calls for further research in controlled environments to test the transition between liquid-like and solid-like behavior.

10.1.5 Inconsistent gap for the sheared zone

In the course of long-duration experiments, a notable phenomenon was observed, namely an incomplete shearing throughout the entire gap between the vane edge and the inner surface of the container. The observation indicated that shearing predominantly took place in the immediate vicinity of the vane, resulting in the formation of a localized sheared region around the vane. This observation is visually demonstrated in figure 10.1.

It is crucial to acknowledge the presence of the Weissenberg effect in figure 10.1, as it introduces challenges in drawing definitive conclusions based solely on visual observations. Nonetheless, a discernible pattern emerges, suggesting the existence of a narrow gap between the innermost and outermost regions. The inner region exhibits spinning motion and undergoes significant shear as a result of the rotational movement of the vane and rod. In contrast, the outermost region appears to remain relatively stationary.

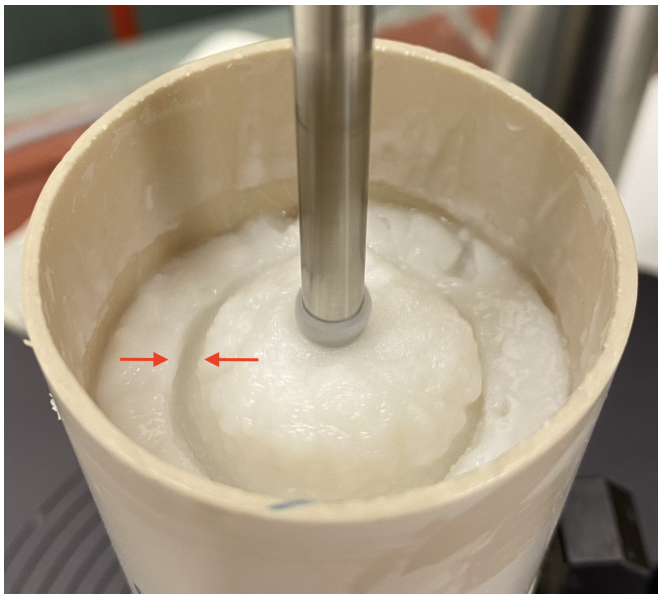

Figure 10.1: Inconsistent sheared gap for an experiment conducted on Exilva with a concentration of 3.60%. The red arrows mark a gap between the inner sheared region and the outer region which appeared to not be sheared. Solidified material is seen on the inner walls of the container.

These observations could potentially establish a hypothesis that the outer region does not experience shearing. This entails that the application of the gap correction factor, for shear stress and shear rate, as outlined in section 4.5.4, becomes invalid. This is due to the fact that the sheared zone no longer extends between the radius of the vane and the radius of the container. Consequently, the radius of the container, R_2, would require adjustment prior to any subsequent calculations.

This hypothesis is challenged by the fact that this type of shearing was only observed during long-lasting experiments with the 3.60% concentration, indicat-

ing that this applies mostly to highly viscous materials. In addition, it may be further induced by the previously discussed evaporation. Verification of whether the material beneath the surface is moving and being sheared, is challenging, as the material is completely non-transparent, and thus a transparent container wouldn't solve the problem. As of the completion of this thesis, no definitive solution or methodology has been identified to address the aforementioned question.

Further, the question is raised whether the utilized rheometer is in fact suitable for testing materials with such plastic behavior. From the available materials for this thesis, only the V40/20 vane was capable of producing results. The V10/5 vane was too small to be verified by the effective dimensions method, while the larger V80/40 vane was too large for the highly viscous material, thus yielding too much resistance for measurements to fall within the reliable range of the Brookfield instrument. The common denominator of these vanes is that they all have a height that corresponds to twice the diameter, or four times the radius. It could be postulated that utilizing a vane with a radius in close proximity to that of the container could potentially yield more reliable calculations. This is attributed to the smaller sheared gap that would result, in reducing the reliance on the gap correction factor in the calculation process. Other vane dimensions, including vanes with other ratios between height and radius, could be used in future work to investigate whether the calculated shear stress and shear rates from this thesis are in fact reliable.

10.1.6 Hysteresis loop and breakdown of initial structure

Across all concentrations investigated, the experimental observations consistently demonstrate the emergence of hysteresis loops. Additionally, the ramp-up curves commence at higher shear stress compared to the termination points of the ramp-down curves. The existence of these distinctive trends suggests the progressive disruption of the initial structural arrangement within the material during the course of the experiments. These outcomes align with the outcomes reported in prior studies conducted on MFC suspensions [47] [14].

10.2 Pipe testing rig

10.2.1 Pipe length

Pipe dimensions are one aspect to consider when analyzing experimental data. The presence of the pipe length as a linear term suggests that longer pipes can contribute to improved consistency and reduced noise in the data. This observation highlights the importance of carefully selecting the appropriate pipe length in order to optimize the experimental setup and mitigate any undesired variations or disturbances.

The Herschel-Bulkley parameters were individually calculated for each pipe length and diameter in an attempt to investigate the potential impact of these param-

eters on the calculations. While some variations were observed, the limited number of specific setups precluded drawing definitive conclusions regarding the actual effects. Including all experiments in the calculations was a deliberate decision aimed at increasing the applicability and generalizability of the model.

Future research should involve conducting multiple parallel experiments using the same setup to explore which parameters may influence the estimation of the Herschel-Bulkley parameters. Furthermore, conducting additional parallel experiments will provide insights into the level of reproducibility of the results. By conducting such studies, a better understanding of the factors affecting the estimation of the Herschel-Bulkley parameters can be achieved, contributing to improved accuracy and reliability of the model.

10.3 Rotational rheometer vs pipe rig

The obtained results demonstrate that for materials with lower concentrations, specifically Exilva at concentrations of 1.86% and 2.44%, the Herschel-Bulkley model based on both rheometer apparent viscosity and the pump rig yields similar outcomes. Although some variations are observed, particularly in the estimation of yield stress, the results exhibit a high level of agreement across the range of tested shear rates.

The consistency between the two methods suggests that the rheometer's apparent viscosity and the pump rig provide comparable information regarding the flow behavior of these lower-concentration materials. Overall, the results indicate a strong agreement between the Herschel-Bulkley model calculations based on rheometer apparent viscosity and pump rig measurements for lower-concentration materials. This finding indicates that either of these methods can be employed to accurately characterize the rheological properties of such materials.

Unfortunately, significant deviations between the methods were observed for materials with higher concentrations, specifically Exilva at a concentration of 3.60%. In this case, either the pump rig overestimated the rheological properties, or the rheometer underestimated them. These discrepancies are noteworthy and indicate challenges in accurately characterizing the rheological behavior of materials at higher concentrations.

Considering the high level of conformity observed between the rheometer data and pipe rig data at lower concentrations, it can be inferred that the pipe rig method yields more reliable and accurate results in this case. The rheometer method encountered several challenges, as previously discussed, when testing materials with higher concentrations, leading to less accurate estimations of the rheological parameters.

10.3.1 Model fitting - Ramp-up vs ramp-down

For all experiments on all concentrations, the ramp-up provided higher shear stress than the ramp-down, at the same shear rates.

The Herschel-Bulkley model was utilized to determine the flow parameters, including the flow consistency index, K, the flow index, n, and the yield stress τ_0. Models were computed separately for the ramp-up and ramp-down data. However, for the 3.60% concentration, only the ramp-up data proved to be consistent enough to generate a reliable model. Specifically, the shear rate varying from 0.1 s^{-1} to 25 s^{-1} was used for this concentration.

Both the ramp-up and ramp-down models from the rheometer exhibit a tendency to underestimate the experimental data at extremely low shear rates, particularly when approaching the limit of zero shear rate.

Comparing the ramp-up and ramp-down models, it is evident that the ramp-up captures more of the initial breakdown of structure and yield stress, as expected. In contrast, the ramp-down data fails to capture this initial breakdown since the structure has already been disrupted. However, the ramp-down data tends to exhibit smoother behavior with reduced noise compared to the ramp-up data. These findings emphasize the differences between the ramp-up and ramp-down data and their respective modeling outcomes. The ramp-up data provides insights into the initial breakdown of structure and yield stress, while the ramp-down data offers smoother trends with reduced noise. Consideration of these factors should be taken when selecting the appropriate data set for analysis, depending on the specific objectives and characteristics of the material under investigation.

10.4 Further research

Further research in the field of rheological characterization can contribute to a deeper understanding of material behavior and improve the accuracy of modeling approaches. Several areas warrant attention for future investigations.

One aspect to consider is the verification of yield stress estimations. Although the Herschel-Bulkley model provides estimates of the yield stress, it is important to validate these estimations through dedicated yield stress tests. Conducting more measurements at very low shear rates, closer to the limit of zero shear rate, could improve the accuracy of yield stress estimation. Exploring alternative measurement techniques, such as oscillatory rheology, may also provide complementary information about the material's yield behavior.

The investigation of multiple approaches for determining the apparent viscosity is a crucial endeavor in validating the outcomes. This thesis solely focuses on calculating the apparent viscosity through the direct utilization of non-Newtonian shear rate and shear stress correction factors. An alternative model was initially proposed in conjunction with the employed method. The theory framework

encompassed the description of this alternative approach, however, due to time-consuming challenges encountered during experimental work and the constraints imposed by the thesis timeline, the exploration of the alternative method was regrettably not pursued. Incorporating two distinct methodologies would have facilitated a broader generalization and enhanced the validation of the viscosity results obtained.

Additionally, it is important to investigate the effects of ramp-up duration on the material's structure. Prolonged ramp-up durations may subject the material to higher shear rates for an extended period, potentially leading to the breakdown of time-dependent structures. Conducting experiments with varying ramp-up durations and comparing the resulting rheological properties can provide insights into the impact of ramp-up duration on the material's behavior.

Furthermore, there is scope for exploring the influence of different pumps in the pipe testing rig. Conducting experiments using pumps with varying flow velocities can provide insights into the impact of different flow rates on the material's rheological properties. This would enable a better understanding of how flow velocity affects the behavior of the material and can contribute to the development of more generalized models.

Investigating the effect of different pipe diameters and lengths would also be valuable. Varying the pipe dimensions can provide a broader understanding of how these factors influence the flow characteristics and rheological properties of the material. By considering different pipe geometries, it would be possible to develop more generalized models that can be applied to a range of pipe configurations commonly encountered in practical applications.

Lastly, an area of interest is the time dependency of materials. While the current study focused on steady-state measurements at various shear rates, many materials exhibit time-dependent behavior. Conducting time-dependent experiments, would provide valuable insights into the material's viscoelastic properties and enhance the understanding of its rheological behavior.

11 Conclusion

This thesis aimed to investigate the rheological properties of sewage sludge through a model fluid, Exilva, a microfibrillated cellulose (MFC) material. The investigation happened through rheometer testing and pipe rig experiments. The discussion section encompassed three main areas: the rheometer analysis, the pipe rig testing, and a comparison between the two methods.

The rheometer analysis revealed that Exilva exhibited non-Newtonian shear thinning behavior, where higher concentrations lead to higher shear stress and viscosity. These findings aligned with previous research and information from the producer, validating the reliability of the data. Additionally, the study highlights the influence of vane dimensions, container size, and submersion depth on the determination of effective dimensions. It was also observed that evaporation and the Weissenberg effect posed challenges during long-duration experiments.

The pipe rig testing yielded significant insights into the flow characteristics of Exilva within a realistic flow environment. The experimental results demonstrated that all concentrations tested could be effectively represented by the Herschel-Bulkley model, and the calculated pressure drops from the model aligned well with the observed values. The experiments also showcased a high level of reproducibility.

The comparison between the rheometer and pipe rig methods demonstrated that, for lower-concentration materials, the Herschel-Bulkley model based on both rheometer apparent viscosity and pipe rig measurements produced similar outcomes. However, when dealing with higher-concentration materials, notable discrepancies were observed, highlighting the challenges in accurately characterizing their rheological properties. Moreover, experiments revealed that the pipe rig approach yielded more reliable results for higher-concentration materials, while the rheometer encountered difficulties in accurately estimating the rheological parameters in such cases.

In summary, this thesis contributes to a deeper understanding of Exilva's rheological properties and its response to different testing methodologies. The findings emphasize the importance of considering various factors, such as vane dimensions, container size, submersion depth, evaporation, and the Weissenberg effect, in experimental setups. Furthermore, the comparison between the rheometer and pipe rig methods highlights the advantages of the pipe rig in accurately characterizing the rheological behavior of higher-concentration materials.

The lab bench rheometer proves effective in estimating the flow of viscous solutions for materials at lower concentrations. However, its performance diminishes when dealing with materials of higher concentrations.

Overall, this study lays the groundwork for future research to further explore and optimize the characterization of highly viscous materials.

References

[1] Pelle Jensen. Rheological characterization of sludge from wastewater treatment plants compared to microfibrillated cellulose suspensions. NTNU, 2022.

[2] Herman F. George and Farrukh Qureshi. *Newton's Law of Viscosity, Newtonian and Non-Newtonian Fluids*, pages 2416–2420. Springer US, Boston, MA, 2013. ISBN 978-0-387-92897-5. doi: 10.1007/978-0-387-92897-5_143.

[3] Nicky Eshtiaghi, Flora Markis, Shao Dong Yap, Jean-Christophe Baudez, and Paul Slatter. Rheological characterisation of municipal sludge: A review. *Water Research*, 47(15):5493–5510, 2013. doi: https://doi.org/10.1016/j.watres.2013.07.001.

[4] F. Dilek Sanin. Effect of solution physical chemistry on the rheological properties of activated sludge. *Water SA*, 28(2):207 – 211, 2002. doi: https://10.4314/wsa.v28i2.4886.

[5] Izrail S Turovskiy and PK Mathai. *Wastewater sludge processing*. John Wiley & Sons, 2006. Chapter 2.

[6] Kevin Hii. Rheological characterisation of thermally hydrolysed waste activated sludge. *RMIT University; Doctor of Philosophy (PhD)*, 2019. doi: https://researchrepository.rmit.edu.au/esploro/outputs/doctoral/Rheological-characterisation-of-thermally-hydrolysed-waste/9921863787501341.

[7] M. C. Collivignarelli, M. Carnevale Miino, S. Bellazzi, F. M. Caccamo, A. Durante, and A. Abbà. Review of rheological behaviour of sewage sludge and its importance in the management of wastewater treatment plants. *Water Practice & Technology*, 17(1):483–491, 2022. doi: https://doi.org/10.2166/wpt.2021.098.

[8] Eugene Hong, Anteneh Mesfin Yeneneh, Tushar Kanti Sen, Ha Ming Ang, and Ahmet Kayaalp. A comprehensive review on rheological studies of sludge from various sections of municipal wastewater treatment plants for enhancement of process performance. *Advances in Colloid and Interface Science*, 257:19–30, 2018. doi: https://doi.org/10.1016/j.cis.2018.06.002.

[9] Flora Markis, Jean-Christophe Baudez, Rajarathinam Parthasarathy, Paul Slatter, and Nicky Eshtiaghi. Rheological characterisation of primary and secondary sludge: Impact of solids concentration. *Chemical Engineering Journal*, 253:526–537, 2014. doi: https://doi.org/10.1016/j.cej.2014.05.085.

[10] N Tixier, G Guibaud, and M Baudu. Determination of some rheological parameters for the characterization of activated sludge. *Bioresource Technology*, 90(2):215–220, 2003. doi: https://doi.org/10.1016/S0960-8524(03)00109-3.

[11] N Tixier, G Guibaud, and M Baudu. Effect of ph and ionic environment changes on interparticle interactions affecting activated sludge flocs: a rheological approach. *Environmental technology*, 24(8):971–978, 2003. doi: https://doi.org/10.1080/09593330309385635.

[12] Borregaard and Exilva. Microfibrillated cellulose and rheology modification: Characteristics and application examples. *Borregaard*, 2022.

[13] Borregaard and Exilva. Microfibrillated cellulose at a glance, characteristics and potential applications. *Borregaard*, 2022.

[14] Marco Iotti, Øyvind Weiby Gregersen, Størker Moe, and Marianne Lenes. Rheological studies of microfibrillar cellulose water dispersions. *Journal of Polymers and the Environment volume*, 19:137–145, 2011. doi: https://doi.org/10.1007/s10924-010-0248-2.

[15] Jean-Christophe Baudez, Rahul K Gupta, Nicky Eshtiaghi, and Paul Slatter. The viscoelastic behaviour of raw and anaerobic digested sludge: strong similarities with soft-glassy materials. *Water Research*, 47(1):173–180, 2013. doi: https://doi.org/10.1016/j.watres.2012.09.048.

[16] Hyun Joo Hwang, Robert A Riggleman, and John C Crocker. Understanding soft glassy materials using an energy landscape approach. *Nature materials*, 15(9):1031–1036, 2016. doi: https://doi.org/10.1038/nmat4663.

[17] Peyronel Fernanda. Chapter 11 - methods used in the study of the physical properties of fats. In Alejandro G. Marangoni, editor, *Structure-Function Analysis of Edible Fats (Second Edition)*, pages 313–385. AOCS Press, second edition edition, 2018. ISBN 978-0-12-814041-3. doi: https://doi.org/10.1016/B978-0-12-814041-3.00011-3.

[18] Uranbileg Daalkhaijav. *Rheological Techniques in Characterization and Aiding in the Modification of Soft Matter*. PhD thesis, Oregon State University, 05 2018.

[19] Haitham M. Ahmed, Bhargav Bharathan, Mehrdad Kermani, Ferri Hassani, Mohammed A. Hefni, Hussin A. M. Ahmed, Gamal S. A. Hassan 1, Essam B. Moustafa, Hussein A. Saleem, and Agus P. Sasmito. Evaluation of rheology measurements techniques for pressure loss in mine paste backfill transportation. *Minerals*, 12(6), 2022. ISSN 2075-163X. doi: https://doi.org/10.3390/min12060678.

[20] C.F. Ferraris and N.S. Martys. 3 - concrete rheometers. In *Understanding the Rheology of Concrete*, Woodhead Publishing Series in Civil and Structural Engineering, pages 63–82. Woodhead Publishing, 2012. ISBN 978-0-85709-028-7. doi: https://doi.org/10.1533/9780857095282.1.63.

[21] H Zhu and D De Kee. Double concentric cylinder geometry with slotted rotor to measure the yield stress of complex systems: A numerical study. *Journal of Rheology*, 52(4):913–922, 2008. doi: https://doi.org/10.1122/1.2936073.

[22] Chengcheng Tao, Eilis Rosenbaum, Barbara G Kutchko, and Mehrdad Massoudi. The importance of vane configuration on yield stress measurements of cement slurry. *NETL*, 2020. doi: https://doi.org/10.18141/1614691.

[23] Alexandre Pierre, Arnaud Perrot, Aymeric Histace, Saber Gharsalli, and E-H. Kadri. A study on the limitations of a vane rheometer for mineral suspensions using image processing. *Rheologica Acta*, 59:351–367, 2017. doi: https://doi.org/10.1007/s00397-017-0993-4.

[24] XD Zhang, DW Giles, VH Barocas, K Yasunaga, and CW Macosko. Measurement of foam modulus via a vane rheometer. *Journal of Rheology*, 42 (4):871–889, 1998. doi: https://doi.org/10.1122/1.550906.

[25] Christophe Baravian, Audrey Lalante, and Alan Parker. Vane rheometry with a large, finite gap. *Applied Rheology*, 12(2):81–87, 2002. doi: https://doi.org/10.1515/arh-2002-0005.

[26] M Keentok. The measurement of the yield stress of liquids. *Rheologica Acta*, 21:325–332, 1982. doi: https://doi.org/10.1007/BF01515720.

[27] J Yan and AE James. The yield surface of viscoelastic and plastic fluids in a vane viscometer. *Journal of non-Newtonian fluid mechanics*, 70(3):237–253, 1997. doi: https://doi.org/10.1016/S0377-0257(97)00005-0.

[28] HA Barnes and JO Carnali. The vane-in-cup as a novel rheometer geometry for shear thinning and thixotropic materials. *Journal of rheology*, 34(6):841–866, 1990. doi: https://doi.org/10.1122/1.550103.

[29] M Keentok, JF Milthorpe, and E O'donovan. On the shearing zone around rotating vanes in plastic liquids: theory and experiment. *Journal of Non-Newtonian Fluid Mechanics*, 17(1):23–35, 1985. doi: https://doi.org/10.1016/0377-0257(85)80003-3.

[30] JD Sherwood and GH Meeten. The use of the vane to measure the shear modulus of linear elastic solids. *Journal of non-newtonian fluid mechanics*, 41(1-2):101–118, 1991. doi: https://doi.org/10.1016/0377-0257(91)87037-X.

[31] Irvin M Krieger and Samuel H Maron. Direct determination of the flow curves of non-newtonian fluids. iii. standardized treatment of viscometric data. *Journal of applied physics*, 25(1):72–75, 1954. doi: https://doi.org/10.1063/1.1721523.

[32] David V Boger and Kenneth Walters. *Rheological phenomena in focus*. Elsevier, 2012. p. 11-19.

[33] Christie John Geankoplis, A. Allen Hersel, and Daniel H. Lepek. *Transport Processes and Separation Process Principles*. Pearson Education, Inc., 2014. ISBN 0-13-101367-X. Chapter 2.

[34] E. Shashi Menon. Chapter five - fluid flow in pipes. In E. Shashi Menon,

editor, *Transmission Pipeline Calculations and Simulations Manual*, pages 149–234. Gulf Professional Publishing, 2015. ISBN 978-1-85617-830-3. doi: https://doi.org/10.1016/B978-1-85617-830-3.00005-5.

[35] Xiao-jun Wang, Thomas E Milner, Zhongping Chen, and J Stuart Nelson. Measurement of fluid-flow-velocity profile in turbid media by the use of optical doppler tomography. *Applied Optics*, 36(1):144–149, 1997. doi: https://doi.org/10.1364/AO.36.000144.

[36] Innokentij Bogatykh and Thomas Osterland. Characterization of residence time distribution in a plug flow reactor. *Chemie Ingenieur Technik*, 91(5): 668–672, 2019. doi: https://doi.org/10.1002/cite.201800170.

[37] Dawid Taler. Determining velocity and friction factor for turbulent flow in smooth tubes. *International Journal of Thermal Sciences*, 105:109–122, 2016. doi: https://doi.org/10.1016/j.ijthermalsci.2016.02.011.

[38] Paul Thomas Slatter. Transitional and turbulent flow of non-newtonian slurries in pipes. *University of Cape Town*, 1995.

[39] Nicky Eshtiaghi, Flora Markis, and Paul Slatter. The laminar/turbulent transition in a sludge pipeline. *Water Science & Technology*, 65(4):697–702, 2012. doi: https://doi.org/10.2166/wst.2012.893.

[40] Christie John Geankoplis, A. Allen Hersel, and Daniel H. Lepek. *Transport Processes and Separation Process Principles*. Pearson Education, Inc., 2014. ISBN 0-13-101367-X. Chapter 3.

[41] K Vamshi Krishna, Kuchi Swathi, Manupati Hemalatha, and S Venkata Mohan. Bioelectrocatalyst in microbial electrochemical systems and extracellular electron transport. In *Microbial Electrochemical Technology*, pages 117–141. Elsevier, 2019. doi: https://doi.org/10.1016/B978-0-444-64052-9.00006-6.

[42] Jean-Christophe Baudez and Philippe Coussot. Rheology of aging, concentrated, polymeric suspensions: Application to pasty sewage sludges. *Journal of Rheology*, 45(1123), 2001. doi: https://doi.org/10.1122/1.1392298.

[43] Farbod Dadgar. Personal communication, 16/5/22. Personal communication about which rheology models are used by Cambi.

[44] Ametek brookfield. `https://www.brookfieldengineering.com/`, 2022. (Accessed on 01/05/2023).

[45] Wade KJ Mosse, David V Boger, and Gil Garnier. Avoiding slip in pulp suspension rheometry. *Journal of Rheology*, 56(6):1517–1533, 2012. doi: https://doi.org/10.1122/1.4752193.

[46] Elias C Aifantis. The physics of plastic deformation. *International journal of plasticity*, 3(3):211–247, 1987. doi: https://doi.org/10.1016/0749-6419(87)90021-0.

[47] Michel Schenker, Joachim Schoelkopf, Patrick Gane, and Patrice Mangin. Quantification of flow curve hysteresis data–a novel tool for characterising microfibrillated cellulose (mfc) suspensions. *Applied Rheology*, 28(2), 2018. doi: https://doi.org/10.3933/applrheol-28-22945.

[48] Detailed information on rheo3000 software. `https://www.brookfieldengineering.com/products/software/rheo3000`, 2022. (Accessed on 11/16/2022).

Appendices

A Rheometer - Rheo300 Programs

Multiple tests were conducted on each sample. The following sections show the programs which were run for each test. All of the programs were created in the Rheo3000 software by Brookfield[48].

A.1 Newtonian fluid - effective dimensions determinations

The constant shear rate tests performed in the Rheo3000 software are referred to as "Modulus" tests. In these tests, a constant shear rate is applied to the sample. The measuring blocks used for conducting constant shear rate tests in Rheo3000 are depicted in Figure A.1.

Figure A.1: Rheo3000 program for testing constant angular velocity

A.2 non-Newtonian fluid - Ramp-up and ramp-down

The controlled shear rate tests conducted in the Rheo3000 software are referred to as "Ramp" tests. These tests involve applying varying shear rates to the sample. The measuring block used for conducting these controlled shear rate tests in Rheo3000 is illustrated in Figure A.2.

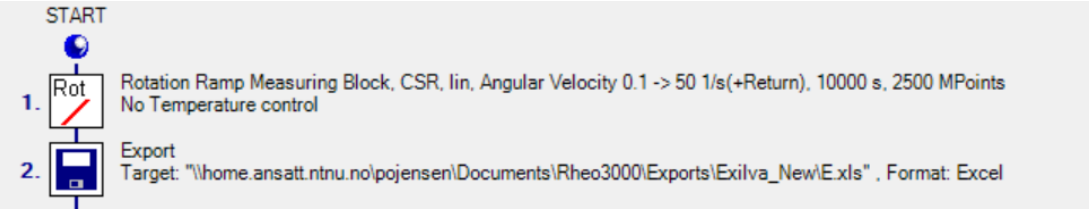

Figure A.2: Rheo3000 program for testing controlled angular velocity

B Python scrips

B.1 Effective height and radius - Newtonian fluids

```
def get_container_data(data, geometry):
    # Creating separate dataframes for each vane and
       container
    data = data[data["Geometry"] == geometry]
    df = data[data["y [cm]"] >= 0]
    df_l = df[df["Container"] == "Large"]
    df_s = df[df["Container"] == "Small"]

    # Large container
    # Creating two arrays with data for optimizing the
       radius
    df_l_x_bar = df_l[['y [cm]','R22 [cm2]']].values
    df_l_y_bar = df_l['LeftSide [cm3]']
    popt_l, pcov_l = curve_fit(func, df_l_x_bar,
       df_l_y_bar, absolute_sigma=True)
    perr_l = np.sqrt(np.diag(pcov_l)) # Standard deviation
        errors

    # Small container
    df_s_x_bar = df_s[['y [cm]','R22 [cm2]']].values
    df_s_y_bar = df_s['LeftSide [cm3]']
    popt_s, pcov_s = curve_fit(func, df_s_x_bar,
       df_s_y_bar, absolute_sigma=True)
    perr_s = np.sqrt(np.diag(pcov_s)) # Standard deviation
        errors

    # Combined small and large
    df_x_bar = df[['y [cm]','R22 [cm2]']].values
    df_y_bar = df['LeftSide [cm3]']
    popt_c, pcov_c = curve_fit(func, df_x_bar, df_y_bar,
       absolute_sigma=True)
    perr_c = np.sqrt(np.diag(pcov_c)) # Standard deviation
        errors

    # Effective radius, effective height, and std for each
        container
    # (l=large, s=small, c=combined)
    R1_l = np.sqrt(popt_l[0])
    H_l = popt_l[1]
    std_R1_l = np.sqrt(perr_l[0])
    std_H_l = perr_l[1]
```

```
    R1_s = np.sqrt(popt_s[0])
    H_s = popt_s[1]
    std_R1_s = np.sqrt(perr_s[0])
    std_H_s = perr_s[1]

    R1_c = np.sqrt(popt_c[0])
    H_c = popt_c[1]
    std_R1_c = np.sqrt(perr_c[0])
    std_H_c = perr_c[1]

    results = {
        'Large container': {'R1': R1_l, 'std_R1': std_R1_l
            , 'H': H_l, 'std_H': std_H_l},
        'Small container': {'R1': R1_s, 'std_R1': std_R1_s
            , 'H': H_s, 'std_H': std_H_s},
        'Combined containers': {'R1': R1_c, 'std_R1':
            std_R1_c, 'H': H_c, 'std_H': std_H_c}}

    return pd.DataFrame(data=results)
```

B.2 Viscosity of Newtonian fluids

```
def calculate_eta(data, geometry, material, container,
    y_error, y_values, R12_mean, R12_std, H_mean, H_std, N,
    n):
    """
    Calculates viscosity (eta) values for different y
        depths for a given geometry, material, and
        container type.

    Parameters:
    ----------
    data : pandas.DataFrame
        The input data
    geometry : str
        The geometry type to consider
    material : str
        The material type to consider
    container : str
        The container type to consider
    y_error : float
        The standard deviation of the error in y
            measurements, cm
    y_values : list
        A list of y values to calculate eta for, cm
```

```
    R12_mean : float
        The mean value of R12
    R12_std : float
        The standard deviation of R12
    H_mean : float
        The mean value of H
    H_std : float
        The standard deviation of H
    N : int
        The number of samples to generate for the Monte
            Carlo simulation
    n : int
        The number of omega, gamma, and depth (they are
            already 4 long)

    Returns:
    ----------
    results : dict
        A dictionary containing the mean and standard
            deviation of eta values for each y depth.
    """
    results = {}

    df_geometry = data[data["Geometry"] == geometry]
    df_material = df_geometry[df_geometry["Material"] ==
        material]
    df_container = df_material[df_material["Container"] ==
        container]

    for y in y_values:
        df_y = df_container[df_container["y [cm]"] == y]
        Omega = np.array(df_y["Angular velocity [1/s]"].
            tolist()*n)
        Gamma = np.array(df_y["Torque [mNm]"].tolist()*n)
        R22 = np.array(df_y["R22 [cm2]"].tolist()*n)
        y_list = np.array(df_y["y [cm]"].tolist()*n)
        R12_arr = np.random.normal(loc=R12_mean, scale=
            R12_std, size=N)
        H_arr = np.random.normal(loc=H_mean, scale=H_std,
            size=N)
        y_arr = np.random.normal(loc=y_list, scale=y_error
            , size=N)
        eta_arr = (Gamma/Omega) * (R22-R12_arr)/(4.*np.pi*
            R12_arr*R22*(H_arr-y_arr))*1000
        mu, std = norm.fit(eta_arr)
```

```
        results[f"y = {y}"] = {"mean": mu, "std": std}
    return pd.DataFrame(data=results)


def plot_eta_results(result1, result2, y_error, label1="
    Result 1", label2="Result 2", title = "title"):
    """
    Plots the mean and standard deviation of eta values
       for each y depth for two different result files.

    Parameters:
    ----------
    result1 : dict
        A dictionary containing the mean and standard
           deviation of eta values for each y depth from
           the first file.
    result2 : dict
        A dictionary containing the mean and standard
           deviation of eta values for each y depth from
           the second file.
    y_error : float
        The standard deviation of the error in y
           measurements, cm
    label1 : str, optional
        Label for the first result file (default: "Result
           1").
    label2 : str, optional
        Label for the second result file (default: "Result
            2").
    title : str,
        title of plot
    """
    x_values1 = []
    y_values1 = []
    y_err_values1 = []
    mean_values1 = []
    std_values1 = []

    for y, data in result1.items():
        x_values1.append(float(y.split(" ")[-1]))
        y_values1.append(data["mean"])
        y_err_values1.append(data["std"])
        mean_values1.append(data["mean"])
        std_values1.append(data["std"])

    x_values2 = []
```

```
    y_values2 = []
    y_err_values2 = []
    mean_values2 = []
    std_values2 = []

    for y, data in result2.items():
        x_values2.append(float(y.split("␣")[-1]))
        y_values2.append(data["mean"])
        y_err_values2.append(data["std"])
        mean_values2.append(data["mean"])
        std_values2.append(data["std"])

    fig, ax = plt.subplots()
    ax.errorbar(x_values1, y_values1, xerr=y_error, yerr=
       y_err_values1, linestyle='None', marker='o',
       capsize=4, label=label1)
    ax.errorbar(x_values2, y_values2, xerr=y_error, yerr=
       y_err_values2, linestyle='None', marker='^',
       capsize=4, label=label2)
    ax.axhline(y = visc_table_value, color = 'r',
       linestyle = '—', label = "CP4/40")
    ax.set_ylabel("Apparent␣viscosity␣[Pa␣s]")
    ax.set_xlabel("y␣[cm]")
    #ax.set_title(title)
    ax.legend(loc=(1.04, 0.5))
    plt.show()
    return fig
```

B.3 Estimation of Herschel-Bulkley parameters - Rheometer

```
def HerschelBulkley(params, x, data=None):
    p=params.valuesdict()
    y_pred=p['tau0']+p['K']*pow(x,p['n'])
    if data is None:
        return y_pred
    else:
        #return mean_squared_error(data, y_pred)
        return data-y_pred

def fit_herschel_bulkley(df_list, materials):
    fit_params = Parameters()
    fit_params.add('K', value=0.2, max=1000, min=0.05)
    fit_params.add('n', value=0.2 , max=0.99, min=0.1)
    fit_params.add('tau0', value=10, max=1000, min=0)
```

```
    results = []

    for material, df in zip(materials, df_list):
        K_value = []
        n_value = []
        tau0_value = []
        timer = []
        method = []
        chisqr = []
        Niterations = []
        #md = ['dual_annealing']
        #md=['dual_annealing','basinhopping', 'leastsq']
        #md=['leastsq','cg','dual_annealing','ampgo','
            nelder','basinhopping','shgo','bfgs','powell','
            differential_evolution']

        for i in md:
            start_time = time.time()
            x = df['Shear rate [1/s]'].values
            data = df['Shear stress [Pa]'].values
            minner = Minimizer(HerschelBulkley, fit_params
                , fcn_args=(x, data))
            result = minner.minimize(method=i)
            dt = time.time() - start_time
            K_value.append(result.params['K'].value)
            n_value.append(result.params['n'].value)
            tau0_value.append(result.params['tau0'].value)
            Niterations.append(result.nfev)
            timer.append(dt)
            chisqr.append(result.chisqr)

        d = {'Material': [material] * len(md), 'Method':
           md, 'N iter': Niterations, 'time(sec)': timer,
           'chi-square': chisqr, \
             'K': K_value, 'n': n_value, 'tau0':
                tau0_value}

        dfres = pd.DataFrame(data=d)
        results.append(dfres)

    return pd.concat(results, ignore_index=True)
```

B.4 Estimation of Herschel-Bulkley parameters - pipe rig

The model fitting was conducted with a confidential Python script. The method is based on work done by, amongst others, Slatter & Co[39]. The model assumes pipe plug flow and calculates the Herschel-Bulkley parameters through optimization steps. Because of confidentiality, the model is presented as a black box model. The model may take in experiments with all pipe lengths, pipe diameters, and flow rates in order to calculate the best-fitting model parameters.

C Dry solids and density measurements

C.1 Dry solids

Table C.1 shows the measurements of dry solids content in Exilva samples.

Table C.1: Measurements of dry solids in Exilva. DS = dry solids.

Aim DS	Actual DS [%]	Average DS [%]
2	1.85	1.86
	1.86	
	1.86	
2.43	2.45	2.44
	2.43	
	2.45	
3.55	3.61	3.60
	3.59	
	3.60	

C.2 Density

Table C.2 shows the density measurements of the Exilva samples.

Table C.2: Measurements of the density of Exilva.

Measured density [%]	Average density $[kg/m^3]$
1.00	1.00
1.00	
1.00	
1.00	1.00
1.00	
1.00	
1.01	1.01
1.01	
1.01	

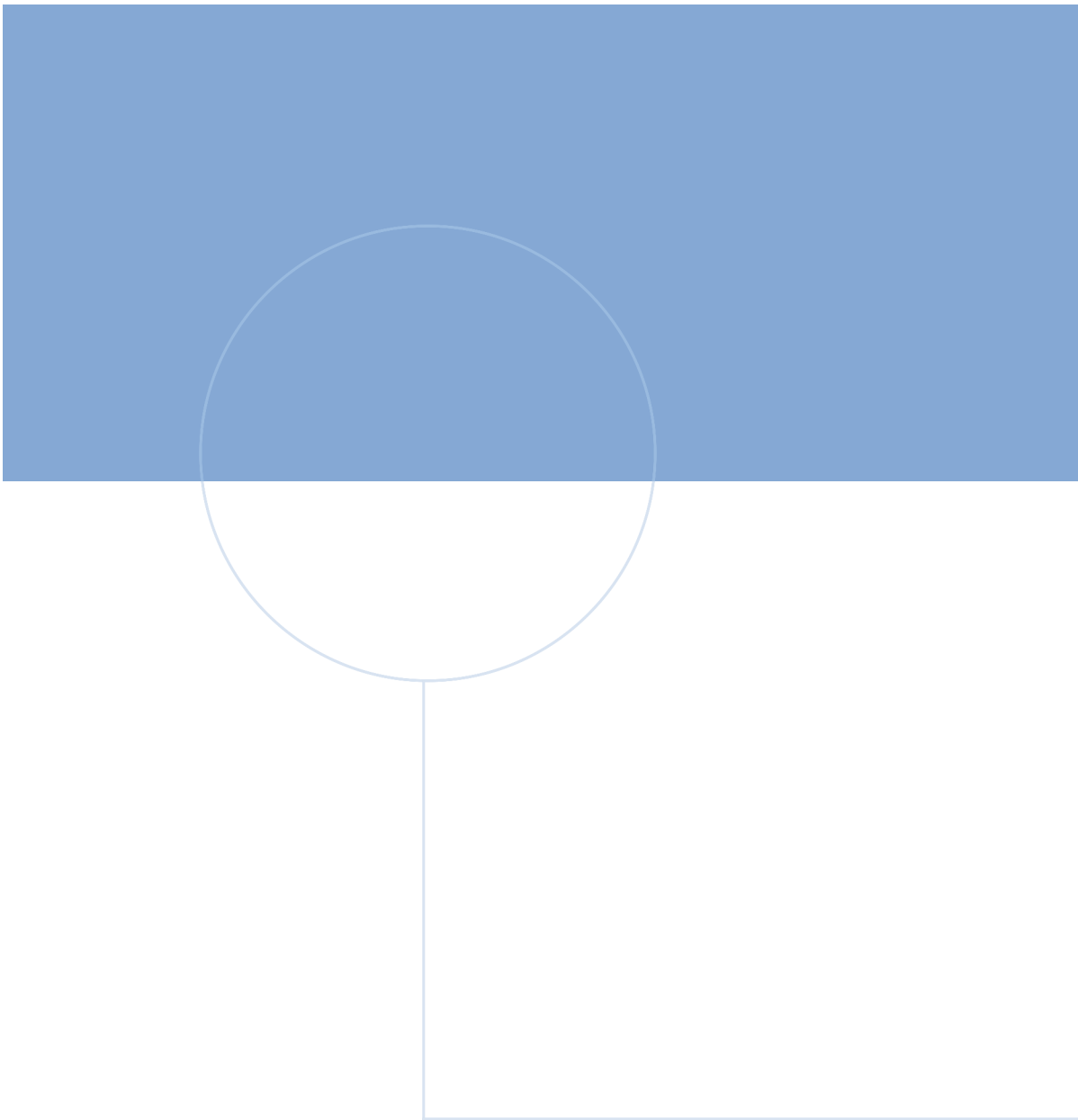

NTNU

Norwegian University of
Science and Technology